UiT
THE ARCTIC
UNIVERSITY
OF NORWAY

Department of Physics and Technology

"Numerical Modeling of Microwave Interactions with Sea Ice"

—

Michael Kampffmeyer

Master thesis in Energy, Climate and Environment EOM-3901 — June 2014

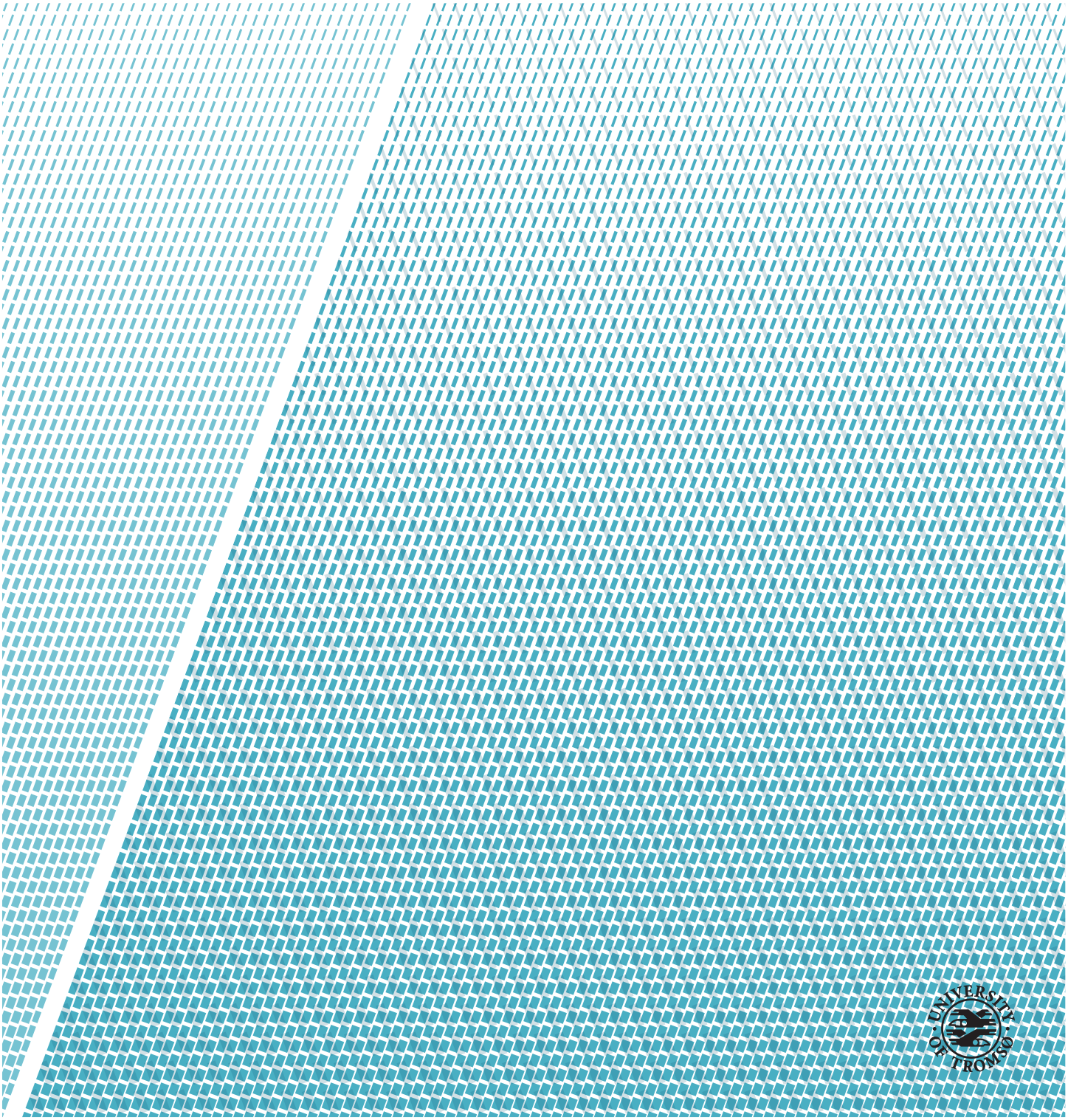

Abstract

Remote sensing is a key instrument for monitoring sea ice surface properties over large areas. Synthetic Aperture Radar (SAR) as well as Real Aperture Radar (RAR) are two types of radars that are extensively used in this context and measure the backscatter of the surface that they illuminate. Backscattering of waves from rough surfaces is complicated and depends, among other things, on the roughness of the illuminated surface and the surfaces material properties.

This thesis focuses on modeling the backscattering cross section from sea ice layers with rough surfaces on top of sea water, by designing a model that builds on the physical basis of electromagnetic wave theory and combines it with the Finite Element Method (FEM) approach. The model is designed as general as possible and can be adapted to various sea ice scenarios by modifying the chosen surface and material properties. Temperature, Density and Salinity (TDS) fieldwork measurements from Van Keulenfjord on Svalbard have been used to estimate realistic continuous permittivity profiles of sea ice using the Polder-van-Santen/de Loor mixture model and have been incorporated into the model.

The model has been validated by comparing its results for a perfectly flat surface to the Fresnel equations and a perfect agreement was achieved. It was also successfully validated using the Bragg scattering phenomena for periodic surfaces. Furthermore, a comparison between the results of the model and the Small Pertubation Model (SPM) was done for a slightly rough surface at different frequencies and permittivities, and clear similarities were observed.

Based on the confidence from the validations, the backscatter cross section of a sea ice/sea water scenario with continuous permittivity profiles has then been modeled.

Acknowledgements

Above all, I would like to express the deepest appreciation to my supervisors Camilla Brekke, Anthony Paul Doulgeris and Frank Melandsø for their guidance and support, and most of all, for the many inspiring discussions during the course of this thesis. Their willingness to give their time so generously has been very much appreciated.

I am grateful to Dr. Cathleen Jones at NASA's Jet Propulsion Laboratory for providing me with the sea water permittivity script that was used in the model and to Anders Carlström at RUAG Space AB for sending me his PhD thesis as well as some of his other papers, which have been of great use. I also wish to thank Stian Normann Anfinsen for pointing me towards interesting and relevant literature on the topics of backscatter modeling and surface generation.

Many thanks also to Linus Andersson, Bertil Nistad and Durk de Vries at the COMSOL Technical Support, who patiently answered my questions regarding the inner workings of COMSOL and to Espen Tangen for support using Stallo.

Finally, on a personal note, I wish to thank the EKM class '09 for five great years, the master's students in the "Norut-brakka" at the auroral observatory for great discussions and Einar Holsbø for proofreading this thesis.

Michael Kampffmeyer
Tromsø, June 2014

Contents

List of Figures

List of Tables

List of Abbreviations

ALOS-2 Advanced Land Observing Satellite-2

ALOS Advanced Land Observing Satellite

DFT Discretized Fourier Transform

FEM Finite Element Method

IEM Integral Equation Surface Backscattering Model

JAXA Japan Aerospace Exploration Agency

PALSAR Phased Array L-band Synthetic Aperture Radar

PBC Periodic Boundary Conditions

PDE Partial Differential Equation

PML Perfectly Matched Layer

RAR Real Aperture Radar

RMS Root Mean Square

SAR Synthetic Aperture Radar

SPM Small Pertubation Model

TDS Temperature, Density and Salinity

TE Transverse Electric

TM Transverse Magnetic

Nomenclature

A Area on ground
A_g Effective area of scatterer
A_t Effective area of antenna
A_u Depolarization factors of an inclusion
$\mathbf{B}$ Magnetic field
B_w Bandwidth
C Correlation function
$\mathbf{D}$ Displacement field
D_a Antenna length
$\mathbf{E}$ Electric field
$\mathbf{E^{inc}}$ Incident electric field
$\mathbf{E^{sc}}$ Scattered electric field
$\mathbf{E_p}$ Far field in direction of field point p
F Functional
G_g Gain of the ground in direction of sensor
G_t Gain of antenna
$\mathbf{H}$ Magnetizing field
$\mathbf{J}$ Free electric current density
$\mathbf{J_s}$ Surface current
L Surface length
$\mathscr{L}$ Differential operator
N Number of points in spacial and spectral domain
P_g Incident power
P_r Received power
P_t Transmitted power
$P_{g'}$ Re-radiated power by ground/scatterer
R Slant range
S Surface enclosing the scattering surface
S_b Salinity of brine
S_i Salinity of sea ice
S_{11} Scattering parameter for Port 1
T Temperature (in °C if not stated otherwise)
V Volume of sea ice
V_b Volume of brine in sea ice
Z_0 Intrensic impedance of free space

ΔR Resolution in range direction
Δx Resolution in azimuth direction
Ω Denotes domain of interest
α Absorption constant
β Phase constant
δ_p Penetration depth
ϵ Complex permittivity
ϵ' Real part of the complex permittivity
ϵ'' Imaginary part of the complex permittivity
ϵ^* Permittivity of the region that surrounds the inclusion
ϵ_0 Permittivity of free space
ϵ_∞ High frequency values of the real part of the complex permittivity
ϵ_h Permittivity of the host material of the medium of interest
ϵ_i Permittivity of the inclusion in the medium of interest
ϵ_m Permittivity of the medium of interest
ϵ_s Limiting static values of the real part of the complex permittivity
ϵ_{brine} Complex permittivity of brine
η Normalized intrinsic impedance
κ Dielectric constant
λ Wavelength
λ_r Wavelength of radar
λ_s Wavelength of surface
μ Permeability
μ_0 Permeability of free space
μ_r Relative permeability
ω Angular frequency of the wave
ϕ Unknown quantity in boundary-value problem
ρ Free charge density
ρ_b Brine density
ρ_{si} Density of sea ice
ρ_s Surface charge
σ Radar cross section
σ^0 Radar cross section
σ_c Conductivity
τ Relaxation time in Debye type equation
θ Incidence angle
θ_B Brewster angle
θ_i Angle of incidence
θ_t Angle of transmission
ζ Ratio of mass of salt in the solid salts and mass of salt in the brine
b_n Gaussian random variable
c Speed of light
d The thickness of the second medium
d_f Fraunhofer distance

f Frequency
f_f Forcing function
h Height above ground
k Wavenumber
k_0 Wavenumber in free space
$\mathbf{k_F}$ Wave vector for Floquet periodicity
l Correlation length
n_1 Refractive indexes of medium 1
n_2 Refractive indexes of medium 2
r_p Reflection coefficient for p-polarized wave
r_s Reflection coefficient for s-polarized wave
s_h Standard deviation of the surface height
t_p Transmission coefficient for p-polarized wave
t_s Transmission coefficient for s-polarized wave
v_i Volume fraction that the inclusions occupy

1 Introduction

1.1 The need for modeling of sea ice

Active microwave remote sensing has historically been the most common observation method when investigating properties of sea ice in the Arctic region. This is because it is superior to other remote sensing methods utilizing shorter wavelengths, which can not penetrate the frequent cloud cover in those regions [Eppler et al., 1992]. Another advantage of active microwave remote sensing is that it allows the observation of sea ice during winter months by providing an illumination source. As a major part of this thesis, a numerical Finite Element Method (FEM) model is developed that can model the backscattering cross section from realistic, rough first year sea ice on top of sea water. It models the sea ice using continuous permittivity profiles that were estimated from fieldwork measurements. To the authors knowledge this has not been done before.

Even though sea ice has been observed for more than 100 years from ships and coastal stations, and by the use of aircrafts after World War II, it was not until the 1980s that satellite remote sensing took over as the most important remote sensing method due to its extensive coverage in remote areas [Sandven et al., 2006]. Initially sensors such as Nimbus, Tiros and the Earth Resources and Technology Satellite (renamed to Landsat) were used, which made use of sensors in the visible and infrared part of the electromagnetic spectrum. Due to the previously named problems with clouds, and the illumination condition, passive microwave systems were soon utilized. Passive microwave systems tend to have a coarse resolution ranging typically from 6 to 30km, and are therefore

mainly employed for global monitoring [Sandven et al., 2006]. Local observations were first possible in 1978 when Seasat was launched, which achieved much better accuracy by making use of active remote sensing, providing high resolution Synthetic Aperture Radar (SAR) images. Active remote sensing is a technique used in many other consecutive satellites such as the ERS-1 and ERS-2 from the European Remote Sensing program, as well as the Canadian satellites RADARSAT-1 and RADARSAT-2 [Sandven et al., 2006]. Recently, on the third of April 2014, a new SAR sensor was launched, called Sentinel-1A, which is the first of a two-satellite constellation that has sea ice monitoring as one of its mission objectives [ESA, 2014].

The study of sea ice extent and properties has become more important in the last decades, due to the fact that sea ice restricts the increased ship traffic in the Arctic and Antarctic regions [Johannessen et al., 2006]. The northern sea route, which shall provide more effective transport of goods from Asia to Europe, is an example for this development since the shipped volume is constantly increasing and since it is crucial to have extensive timely and reliable sea ice information for vessel operations to succeed [Ho, 2010]. Sea ice introduces similar problems to the exploration and exploitation of resources such as Oil and Gas in the Arctic regions as it can cause severe damage to structures such as drilling rigs and oil platforms. Another area, where sea ice properties are being used is the study of climate change, as changes in sea ice cover can be used as indicators of coming climate trends [Serreze and Francis, 2006] [Comiso, 2006].

Sea ice SAR images are typically analyzed by experts, who have extensive understanding of the scattering processes. However, even experts can have difficulties to interpret sea ice areas with absolute certainty. In general, the main method used for verifying SAR observations is the collection of ground truth, which is an expensive and time consuming process. In addition, it is often difficult to gather representative ground truth over the SAR imaging area in the instant that it was taken.

1.2 Objective and contribution

The aim of this work is to use the developments in the field of numerical modeling to build a model that can be used to test assumptions and theories by artificially simulating the backscattering cross section of a sea ice surface.

Even though scattering from rough surfaces has been a field of scientific interest for many years it has not been completely solved analytically. Early work was done by [Rayleigh, 1899] and lead to a criterion that is still widely used to estimate the degree of surface roughness, called the Rayleigh roughness crite-

rion. Further work was done by [Feinberg, 1944], in which the propagation of radio waves over a rough surface was studied, and by [Rice, 1951], who used the perturbation theory for electromagnetic scattering of two-dimensional, randomly rough surfaces. In the following years more work was done both on high-frequency and low-frequency surface approximations and has been summarized in [Beckmann and Spizzichino, 1963], which still is considered one of the most influential books in the field. Due to the lack of an analytical solution and the restrictions of the approximate analytical solutions to the scattering problem, numerical methods have been used to more accurately calculate scattering. The main approaches that have been used for the numerical modeling of scattering from surfaces are the method of moments and the FEM as proposed by [Courant et al., 1943]. The method of moments technique was first proposed in [Richmond, 1965] and [Harrington, 1967], and is based on the idea of discretizing an integral equation into a matrix equation that can be solved. Over the past years, due to an increase in available computational resources as well as parallel processing and, more recently, utilization of the graphics processing unit [Michéa and Komatitsch, 2010], the use of these methods has increased considerably.

In remote sensing radar applications the most widely used methods for the scattering problem are the Kirchhoff Approximation and the Small Pertubation Model (SPM), where the Kirchhoff Approximation is valid for surfaces with large roughness compared to the wavelength and the SPM is used for small roughness surfaces. Both these models only provide approximate solutions, however, and can not be used to obtain analytical solutions. [Fung et al., 1992] suggested a new model called the Integral Equation Surface Backscattering Model (IEM), a model that is more generally applicable to a range of surfaces and that is designed to be valid in the gap between the SPM and the Kirchhoff Approximation. The IEM did, however, rely on a simplifying assumption for the Green's function, which caused problems when modeling bistatic scattering. More recently improved versions like the IEM-B model, introduced by [Fung et al., 2002], have provided further advances in the field of surface scattering models, by correcting these issues.

In addition to the theoretical models some semi-empirical models have been developed that have the theoretical models as their foundation and that include observations from fieldwork measurements to achieve better performance, since the theoretical models often do not agree well with experimental data. One example for such a model, based on the SPM, is presented in [Oh et al., 1992], which includes fully polarimetric observations at L-, C-, and X-band frequencies from a truck-mounted network-analyzer-based scatterometer from the University of Michigan (LCX POLARSCAT) to model scattering from bare soil surfaces. Another semi-empirical model is described in [Dubois et al., 1995]. Using only data from dual polarized systems, it has achieved good results for

bare and sparsely vegetated areas using data from LCX POLARSCAT as well as from RASAM, a truck-mounted radiometer-scatterometer from the University of Bern.

Modeling of sea ice in arctic regions has been performed by, among others, [Johansson and Askne, 1987] who presented a simple approach to model backscattering from ice ridges, which later was extended by [Manninen, 1992], and by [Drinkwater, 1989] who suggested a simple scattering model based on the Kirchhoff scattering theory. Another contribution to the field of sea ice modeling is [Winebrenner et al., 1992], who focused on the modeling of sea ice signatures. More work done in sea ice modeling includes [Carlström, 1995] who attempted to model the complete Synthetic Aperture Radar (SAR) imaging process in addition to the electromagnetic backscattering of a surface by forming empirical relations between in situ measurements and observed backscatter coefficients. Recently, a new analytical formulation of the scattering problem for inhomogeneous media was proposed by [Komarov et al., 2014], which was used to evaluate backscatter from a air/snow/ice scenario and which builds on a new multi-layered formulations of the SPM that was proposed in [Imperatore et al., 2009].

The ultimate objective of this thesis is to provide a model that can be used to help deepen the understanding of the interactions between the electromagnetic waves and the sea ice, but which is also reasonably dynamic so that it can be adapted to different materials and surfaces of varying roughness.

Our immediate contribution to the research field is the generation of a general numerical FEM model for first year sea ice that can analyze the backscattering cross section

- From rough surface multi-layered mediums
- For varying wavelengths (frequencies)
- For mediums of varying permittivities
- Incorporating measurement data for temperature, density and salinity to find continuous permittivity profiles

The model has been validated by using the Fresnel equations and the phenomena of Bragg scattering. Additionally the model was compared to the SPM and showed the correct characteristics, even though the backscattering cross section could not be normalized due to the 1-dimensional surface geometry.

1.3 Structure of the thesis

The thesis is structured in 6 chapters including the introduction.

Chapter 2 provides an introduction to sea ice as a material and is divided into three different parts. The first part discusses the formation of sea ice by reviewing the growth process and by linking the growth process to properties such as the sea ice salinity and porosity. The second part focuses on deformation of sea ice and sea ice roughness caused by these deformations. In the final part of the chapter electromagnetic properties of sea ice are discussed and some of the key research in the field of modeling permittivity of sea ice is reviewed.

Chapter 3 reviews some of the most important principles of SAR imaging, such as the imaging geometry and resolution, and then continues to describes how (sea ice) surface properties effect the imaging results.

Chapter 4 introduces the key theory on which the model has been built by reviewing the relevant principles of the Finite Element Method (FEM). It also discusses the design choices that had to be made to ensure the design of a realistic and useful model, whilst staying in the range of the available computational resources.

Chapter 5 presents the results of a set of example cases that are generated using the model and discusses them. The first four cases are used to validate the model, whereas the final case presents a realistic sea ice scenario.

Chapter 6 summarizes the work and proposes future work to extend the model and its applicability.

2

Sea ice

A thorough understanding of sea ice is very important when trying to design a realistic model for the microwave sea ice interaction. From a remote sensing perspective, the large-scale behaviors of sea ice are usually the most interesting ones, but to understand those and to be able to represent them in a model, it is necessary to also understand the sea ice processes on a smaller scale, such as the evolution of the sea ice structure during its growth process. [Petrich and Eicken, 2010] uses a fitting analogy to describe this approach, by stating that to see the forest, which in our case is the backscattering properties, it is important to also see the trees, which are key processes of the sea ice such as the growth process and the inclusion structure of brine. Section 2.1 introduces these small scale processes by providing an overview over the structure of sea ice and its formation. Section 2.2 then describes some of the processes causing deformation of sea ice, before section 2.3 expands on how these formation and deformation processes effect the electromagnetic properties of sea ice.

2.1 Formation of sea ice

This section introduces the general processes involved in the growth of sea ice starting with the crystal structure (section 2.1.1) and the growth process (section 2.1.2). The second part of the section focuses on how the salinity and the porosity of sea ice are affected by the growth. It then shows a simple model that is commonly used to estimate sea ice growth, to illustrate how sea ice is

often accompanied by other layers such as snow.

2.1.1 Crystal structure

When sea water freezes to create ice, the water molecules arrange themselves in a tetrahedral geometry with a 6-fold rotational symmetry in a plane called the basal plane. The plane normal to the basal plane is called the principle crystallographic axis (c-axis), and denotes the axis of maximum rotational symmetry. One important difference between those planes is that the c-axis interface is rough at a molecular level, whereas the basal plane is considered smooth, which causes the ice crystals, also called frazil, to generally grow faster in the basal plane [Petrich and Eicken, 2010].

This specific ice crystal structure allows only a very small group of ions and molecules to be integrated, in which the main ions contained in sea water are not included. This means that they will not be integrated into the crystal structure during the freezing process, but instead create either small brine inclusions, which are liquid inclusions of salt resolved in water, or drain away into the underlying sea water [Petrich and Eicken, 2010].

2.1.2 Sea ice growth

As more and more of these frazils form, a loose mixture of unconsolidated crystals is formed, which is commonly referred to as grease ice. In a continuing freezing process, during calm freezing conditions, the separate crystals begin to freeze together, which results in a solid cover called nilas that can increase to up to 10cm in thickness. In many cases, however, the formation of sea ice is affected by external forces such as wind and waves. This can lead to different phenomena, where the external forces cause for example the accumulation of semi-consolidated frazil in form of little circular masses called pancake ice. Eventually, as the freezing process continues, the open areas between the pancakes will consolidate and also form a solid layer [Tucker III et al., 1992].

Once an sea ice layer has been established, the ocean is insulated by it from the atmosphere and all growth will happen under the insulating ice layer. As the growth phase continues, the layers increase in thickness as seawater freezes to the bottom of the ice due to the fact that heat is transferred upwards through the ice layer by conduction [Tucker III et al., 1992]. The growth rate is therefore determined by the temperature gradient in the layer, the difference between the cold air on the surface and the warm ocean below, and its conductivity. The individual ice crystals also lose one degree of growth freedom, since growing

can only continue without interfering with neighboring crystals as long as the boundary is exactly perpendicular to the growth direction. Due to this there will be a geometric selection, where crystals that are oriented correctly, or very close to the correct inclination, will eliminate the others by cutting them off from the seawater [Tucker III et al., 1992]. The layer caused by this growth process is called the transitional layer, which is commonly completed after 5 to 10 cm of growth, but can in certain cases (with thick layers of frazil) be still in process at one meter below the top sea ice surface. Once the transition layer has formed the growth continues in a columnar fashion forming a columnar zone [Weeks and Ackley, 1986].

As the freezing process continues and the sea ice layer starts to build up in depth, a saline layer is formed at the ice-water interface. This saline water layer has a higher salinity than the sea water due to the salts that are drained out of the sea ice and can vary from a few millimeters in thickness to a few centimeters. This causes a diffusion of salt from the saline layer to the sea water. According to the thermal equilibrium condition, it is known that the interface needs to be at a freezing point. It is, however, also known that the freezing point decreases as salinity increases, causing the interface to be colder than the ocean and resulting in a thermal flux towards the interface [Petrich and Eicken, 2010].

2.1.3 Salinity

The shape of salinity profiles of sea ice in different times of the year can be seen in Figure 2.1. The figure is taken from [Malmgren et al., 1927], a ground breaking study in sea ice properties, which was done as part of the Maud expedition that froze in for nearly two years. It clearly shows the characteristic C-shape profile for the young and first year sea ice, as well as the decrease in surface salinity in the late spring or early summer months due to melt water flushing. During the first summer this process continues and the sea ice looses a great deal of its salinity as it changes over into the class of multi-year ice at the end of the summer. Multi-year sea ice will, during the winter months, experience an increase in relative salinity, but due to its heat conductivity, which is far less than for first year sea ice, the growth process will not continue as rapidly and the salinity of the new formed ice under the multi-year sea ice layer will not be as high as it would be for first year ice. The air and brine content of the sea ice is very important when discussing sea ice in a remote sensing context, since it has large effects on the permittivity and reflectivity.

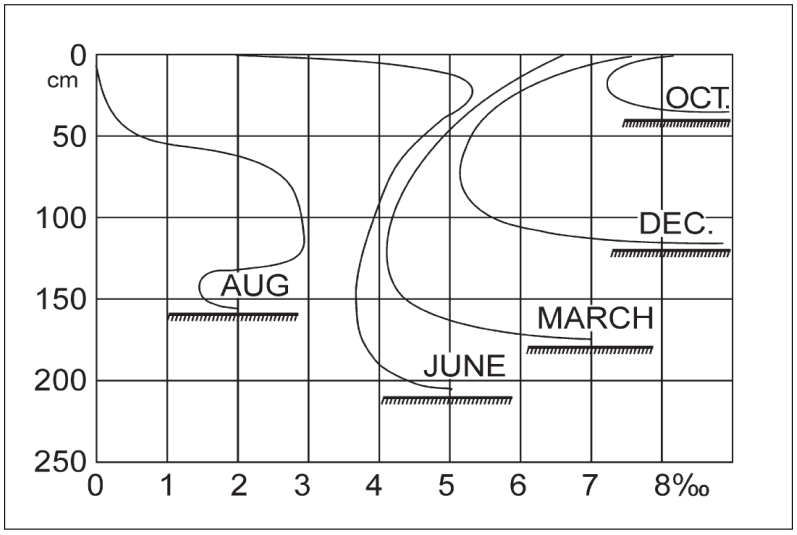

Figure 2.1: Typical development of salinity profiles for first-year sea ice before turning into multi-year sea ice. [Malmgren et al., 1927].

2.1.4 Porosity

To be able to generate a realistic sea ice model it is important to have knowledge about the porosity of sea ice, which has a big impact on sea ice emissivity. As mentioned in section 2.1.1 brine inclusions will be contained in the sea ice layer, but additionally to the brine inclusions, air inclusions will also form as the ice grows older due to the brine draining away. In fresh first year sea ice, however, the volume of the brine inclusions can be assumed to be much larger than the volume of the air inclusions [Petrich and Eicken, 2010].

Porosity of sea ice is usually found by taking in situ measurements for the salinity, density and temperature of the ice. This is done by taking a fresh ice core and measuring the temperature in holes that are drilled into the core at constant intervals. The core is then divided into sections, which are measured and weighed (to calculate density) and then melted in a lab. The salinity can then be found by taking electrolytical conductivity measurements of the melted sea ice sections [Petrich and Eicken, 2010].

Using these measurements in

$$\frac{V_b}{V} = \frac{\rho_{si} S_i}{F_1(T)} \tag{2.1}$$

it is possible to calculate the relative brine volume $\frac{V_b}{V}$, where ρ_{si} is the density,

S_i the salinity and V the total volume of the sea ice. V_b is the volume of the brine, and $F_1(T)$ is an empirical polynomial function of the type

$$F_1(T) = \alpha_0 + \alpha_1 T + \alpha_2 T^2 + \alpha_3 T^3 \,, \tag{2.2}$$

which approximates

$$F_1(T) = \rho_b S_b (1 + \zeta) \,, \tag{2.3}$$

where ρ_b is the brine density, S_b the salinity of the brine, ζ the ratio of mass of salt in the solid salts and mass of salt in the brine, and T the temperature. The coefficients α_0 and α_1,α_2 and α_3 have been determined by [Cox and Weeks, 1983] and can be found in Appendix A together with a more detailed explanation of equation (2.1).

2.1.5 Simple sea ice model

Figure 2.2 shows a simple model that is commonly used to measure sea ice growth with good accuracy [Petrich and Eicken, 2010]. It shows that it is not enough to just look at atmosphere/sea water and sea water/sea ice interaction since the ice is covered by a snow layer during a large part of the year. For ice growth this layer is important as it provides the sea ice with an isolation blanket during the winter and an high albedo during the summer. During the summer, additional changes to the layer structure are caused by melt ponds and pools of open water on the ice surface.

2.2 Deformation of sea ice

This section considers deformation of sea ice and the related roughness features found in sea ice.

2.2.1 Ridges and leads

External forces such as wind and ocean currents keep ice in motion, causing significant deformation of the sea ice with time. Ridges are one of the features

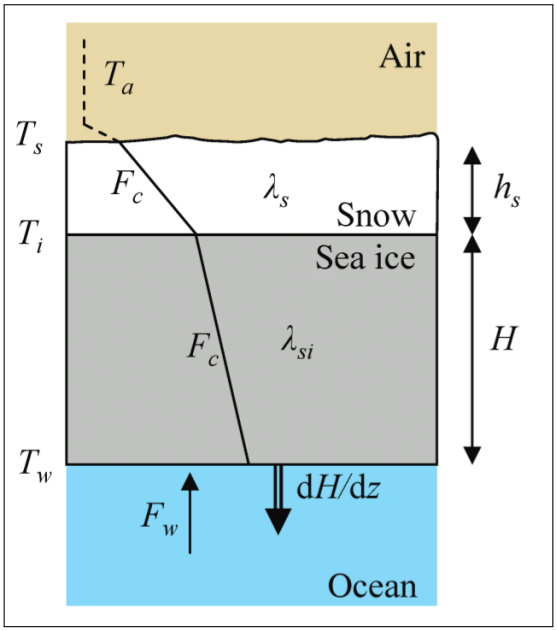

Figure 2.2: Illustration of a simple model for sea ice growth, where λ denotes the thermal conductivity, T the temperature and F the heat flux [Petrich and Eicken, 2010].

that originate from these forces, as sea ice is broken up under shear stress and compression and the resulting blocks are piled on top of each other along a line and consolidate. The majority of ridges form from sea ice that is less than a meter in thickness, but ridges made of thicker ice is not uncommon [Tucker III et al., 1992]. Initially first year ridges consist of very angular blocks, but as a ridge gets older and transforms to a multi-year ridge, weathering sets in and the edges of the blocks get rounder and the ridges height decreases. Extended ridging can lead to rubble fields, where the blocks cover large areas in an unordered fashion.

Open water leads are another phenomena that can be caused by these external forces, as the ice breaks up and diverges leaving large linear fractures in the ice. Figure 2.3 illustrates the generation of leads, which are caused by divergence, and ridges, which are caused by compression.

2.2.2 Surface roughness

Only a few measurements of small scale surface roughness have been conducted. For example [Drinkwater, 1989], based on first-year ice measurements from the Labrador sea ice margin experiment, suggested that the roughness may

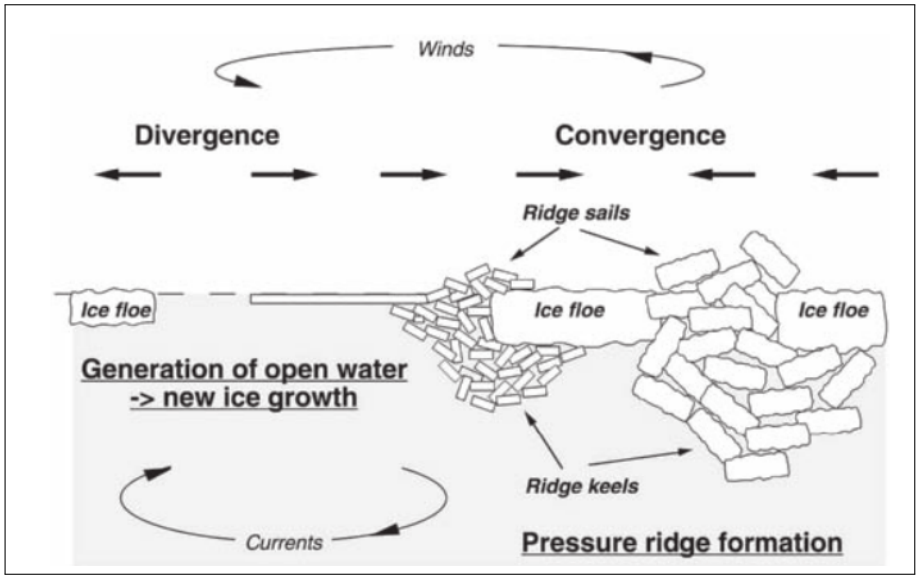

Figure 2.3: Generation of ridges and open water leads by winds and ocean currents [Haas, 2010].

Table 2.1: Height standard deviation and the correlation length of sea ice surfaces found in the literature

	Smooth		Rough		
Article	$s_h[cm]$	$l[cm]$	$s_h[cm]$	$l[cm]$	Location
[Drinkwater, 1989]	1.74	12.8	4.43	18.6	Labrador Sea
[Paterson et al., 1991]	0.78	-	5.26	-	Labrador Sea
[Kim et al., 1985]	0.15	8.9	0.37	8.5	Beaufort Sea
[Onstott, 1992]	0.05	0.5	0.49	3.7	Eastern/Western Arctic

[a] s_h is the standard deviation and l the correlation length

be approximated by either an exponential, or a Gaussian correlation function for undeformed ice floes and deformed sea ice, respectively. Table 2.1 contains an overview over the Root Mean Square (RMS) height (assuming the mean surface height as a reference height) and the correlation length from various experiments and areas. It can be noted that the roughness of smooth first year sea ice varies considerable at different locations due to the variability in strength of the various forces acting on it.

2.3 Electromagnetic properties of sea ice

Expanding on the discussion in the previous section, this section discusses the electromagnetic properties of sea ice related to remote sensing. The intensity of the electric field of a electromagnetic wave propagating along the z-direction at point z can be expressed as

$$E(z) = E_0 e^{-(\alpha + j\beta)z} \,, \tag{2.4}$$

where α is called the absorption constant and describes the amount of energy that is converted to other forms of energy such as heat, and β is the phase constant [Hallikainen and Winebrenner, 1992]. Both these terms are related to the complex permittivity, which is denoted as

$$\epsilon = \epsilon' - j\epsilon'' \,, \tag{2.5}$$

and which governs a mediums electrical properties such as how a wave propagates and how it is attenuated. The real part, ϵ', describes the contrast with regards to the permittivity of free space, whereas the imaginary part, ϵ'', denotes the electromagnetic loss of the material. The aforementioned relationship is

$$\alpha = k_0 |\Im \sqrt{\epsilon}| \tag{2.6}$$

$$\beta = k_0 \Re \sqrt{\epsilon} \,, \tag{2.7}$$

where k_0 is the wavenumber in free space and $\Im$ and $\Re$ denote the imaginary and the real part, respectively. It is important to highlight that both the real and imaginary part of ϵ are frequency dependent in materials that consist of molecules exhibiting a permanent dipole moment, such as for example sea ice and sea water [Petrich and Eicken, 2010].

These properties can be used to calculate another property that is important for remote sensing, namely the penetration depth. This quantity indicates the depth at which the intensity of the incoming wave has attenuated to $\frac{1}{e}$ of its original intensity. Assuming that a medium is homogeneous and that no scattering occurs, the penetration depth, δ_p, can be found as [Hallikainen and Winebrenner, 1992]

$$\delta_p = \frac{1}{2\alpha} = \frac{\sqrt{\epsilon'}}{k_0 \epsilon''} \quad \text{for } \epsilon'' << \epsilon' \,. \tag{2.8}$$

2.3.1 Modeling of the complex permittivity of sea ice

There have been several studies considering the modeling of the complex permittivity of sea ice. One of the early attempts was [Vant et al., 1978], who

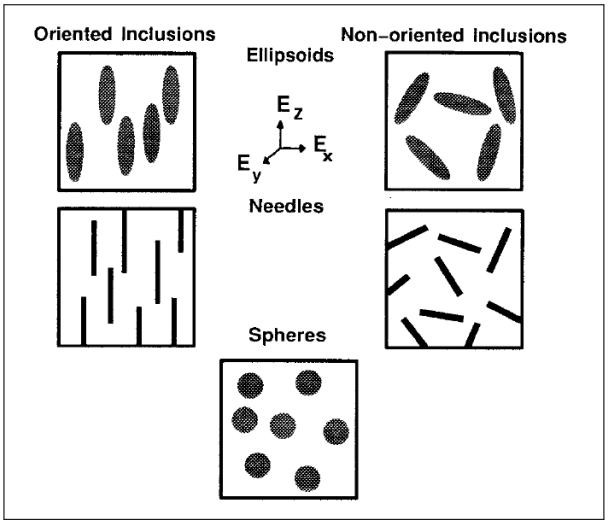

Figure 2.4: Idealizations of different inclusion shapes found in sea ice [Shokr, 1998].

developed a set with empirical equations from a large set of both artificial and natural measurements that linked the sea ice permittivity to the brine volume. In [Hoekstra and Cappillino, 1971] a dielectric mixture model is used to model the permittivity as a mixture of a host material (pure ice) with inclusions (brine). This model is based on the Polder and Van Santen model [Polder and Van Santeen, 1946], which has been modified by [De Loor, 1968] and was evaluated by [Hallikainen, 1977] and [Shokr, 1998]. The Polder-van-Santen/de Loor mixture model is

$$\epsilon_m = \epsilon_h + \frac{v_i(\epsilon_i - \epsilon_h)}{1 + A_u(\frac{\epsilon_i}{\epsilon^*} - 1)} , \tag{2.9}$$

where ϵ_m is the permittivity of the medium of interest, ϵ_h the permittivity of the host material, v_i the volume fraction that the inclusions occupy, ϵ_i the permittivity of the inclusions, A_u the depolarization factors of the inclusion along its axes, and ϵ^* the permittivity of the region that surrounds the inclusion. As a general rule of thumb ϵ^* can be chosen equal to ϵ_h when the inclusions make up less than 10%, since it can be assumed that the interaction between the inclusions can be neglected [Shokr, 1998].

[Shokr, 1998] discusses some of the typical inclusion shapes that sea ice can have (Figure 2.4), and discusses the corresponding depolarization factors and what solutions for the specific cases look like. Of special interest in this thesis are the oriented needle inclusions, which can be found in well developed first year sea ice due to the columnar growth that was discussed in section 2.1.2. The reader is referred to the article for more information.

Adapting the model to sea ice, as was done in [Shokr, 1998], means that ϵ_h is the permittivity of pure/lake ice, whereas ϵ_i is the permittivity of the actual brine solution and v_i is the relative brine volume described in section 2.1.4.

There exist several empirical equations to estimate the complex permittivity of pure/lake ice at a given temperature T and at a given frequency f. Two equations that have shown to fit well with experimental data are [Matzler and Wegmuller, 1987]

$$\epsilon' = 3.1884 + 0.00091T \tag{2.10}$$

to estimate the real part of the complex permittivity, and [Nyfors, 1982], [Rees, 2005]

$$\epsilon'' = 57.34(f^{-1} + 2.48 \cdot 10^{-14} f^{1/2}) e^{0.0362T} \tag{2.11}$$

to estimate the imaginary part of the complex permittivity.[1]

The dielectric properties of brine in sea ice at microwave frequencies is discussed in [Stogryn and Desargant, 1985], which includes a Debye type relaxation equation that can be used to find the permittivity, that is, the ϵ_i in equation 2.9. The model proposed in [Stogryn and Desargant, 1985] is

$$\epsilon_{brine} = \epsilon_\infty + \frac{\epsilon_s - \epsilon_\infty}{1 - j2\pi f\tau} + j\frac{\sigma_c}{2\pi\epsilon_0 f} , \tag{2.12}$$

where ϵ_∞ and ϵ_s correspond to the high frequency and limiting static values of the real part of the complex permittivity ϵ_{brine}, σ_c is the ionic conductivity of the salts and τ is the relaxation time. According to [Stogryn and Desargant, 1985] these parameters are independent of frequency and instead only dependent on temperature. The paper also includes empirical equations for these parameters, where τ in nanoseconds is found using

$$2\pi\tau = 0.10990 + 0.13603 \cdot 10^{-2}T + 0.20894 \cdot 10^{-3}T^2 + 0.28167 \cdot 10^{-5}T^3 \tag{2.13}$$

and σ_c is found using

$$\sigma_c = \begin{cases} -Te^{0.5193+0.8755\cdot 10^{-1}T}, & \text{for } T \geq -22.9°\text{C} \\ -Te^{1.0334+0.1100T}, & \text{for } T < -22.9°\text{C} \end{cases} . \tag{2.14}$$

The rest of the Debye parameters are found using the following equations

$$\epsilon_s = (939.66 - 19.068T)/(10.737 - T) \tag{2.15}$$

$$\epsilon_\infty = (82.79 + 8.19T^2)/(15.68 + T^2) . \tag{2.16}$$

1. The temperature T in equation 2.11 is in Kelvin

By combining these parameters in the model for sea ice permittivity (equation (2.9)), it is thus possible to estimate sea ice permittivity at a frequency f, given a brine volume, which is the inclusion volume v_i, and a temperature T.

3

Synthetic Aperture Radar Imaging

In this chapter the underlying principles of SAR are introduced. They include, among others, the imaging geometry, the spatial resolution, the frequency and polarization. Section 3.2 will expand the idea of SAR by discussing how (sea ice) surface properties affect the observations.

3.1 SAR principles

SAR is an active sensor system that generates and records energy pulses in the microwave spectrum. It is therefore not affected by atmospheric effects such as clouds, and does not require an external illumination source [Chuvieco et al., 2009]. SARs can be divided into two main classes: mono-static radars, where the transmitter and receiver share a common antenna; and bi-static radars, where the transmitter and receiver are separated from each other by a considerable distance. Prior to SARs, Real Aperture Radars (RARs) were used for airborne studies. However, since the spatial resolution depends on the distance between sensor and surface, which is explained in section 3.1.3, it was found to not be practical for satellites. SAR circumvents this drawback by artificially synthesizing a virtual long antenna by making use of the Doppler effect.

3.1.1 Radar equation

The radar equation is an equation that expresses the fundamental idea with radar systems, which is that the generated energy pulses interact with the ground and are scattered back to the sensor where they are recorded.

To establish a link between the emitted power and the backscattered power the total power that is incident on the scatterer needs to be considered [Elachi and Van Zyl, 2006]. It is

$$P_g = \frac{P_t A_g G_t}{4\pi R} \ , \tag{3.1}$$

where P_g is the power incident on the ground (scatterer), A_g is the effective area of the scatterer, P_t is the power transmitted by the sensor, G_t is the gain of the antenna, and $\frac{1}{4\pi R}$ is the factor representing the decrease in power density over the slant range R.

The expression for incident power at the sensor, assuming that the sending and receiving sensors are the same, is given by

$$P_r = \frac{P_{g'} A_t G_g}{4\pi R} \ , \tag{3.2}$$

where P_r is the power received by sensor, A_t the effective area of the antenna $\left(\frac{G_t \lambda^2}{4\pi}\right)$, $P_{g'}$ the re-radiated power by the ground, G_g the gain of the ground in direction of the sensor, $\frac{1}{4\pi R}$ the factor representing the decrease in power density and λ the wavelength.

Using these two equations it is possible to solve for the relationship between P_t and P_r, which results in what is referred to as the radar equation

$$P_r = \frac{G_t^2 \sigma \lambda^2}{(4\pi)^3 R^4} P_t \ , \tag{3.3}$$

where P_r is the power received by sensor, P_t the power transmitted by the sensor, G_t the gain of the antenna, and σ the radar cross section, which is discussed in section 3.2.2.

3.1.2 Imaging geometry

The pulses in a SAR system are sent out perpendicularly to the direction that the carrier platform is traveling as displayed in Figure 3.1a. These pulses are used to image narrow strips on the surface, where the direction perpendicular to the flight path is called the range. The range is determined by taking into

consideration the time it takes for reflections to reach the sensor. This can be done since the travel time is proportional to the distance that the pulse has traveled and therefore in theory provides the distance in range direction. However, this is only correct in theory since mountains or high objects might cause geometric distortions [Chuvieco et al., 2009]. Figure 3.1b shows the geometry on the surface and indicates that the general incidence angle is not necessarily the angle at which the pulses approach the surface. Over time, as the satellite passes by, the image strips that are produced, are stitched together to form an image. This produces an image that is much larger in flight path direction (azimuth) than each individual image strip.

3.1.3 Spatial resolution

Spatial resolution denotes the smallest object that can be detected once the image has been produced [Chuvieco et al., 2009]. When discussing radar resolution it is important to consider azimuth and range directions separately due to the fundamental differences in the way that the images are collected.

In a Real Aperture Radar (RAR) image two objects can only be distinguished in range direction if their scattered and returning pulse arrive at different times back at the sensor. Hence, to allow for objects to be distinguishable the range resolution must be approximately equal to $\frac{\tau}{2}$ where τ is the the pulse length. This means, that pulses should be shortened as much as possible to receive very good resolution, however, this would lead to the need to increase the amplitude to keep the energy signal that is received strong enough to distinguish it from the noise.

It is difficult to design systems that effectively transmit short high amplitude pulses and the chirp principle is therefore used to solve the problem by sending out a frequency modulated signal. Signal processing is then used to refine the resolution [Elachi and Van Zyl, 2006].

Considering the azimuth direction and its resolution, it is known that objects can only be separated when they are not in the radar beam at the same time, thus when the distance between them is larger than the beam-width of the radar. This means, that for RAR the resolution in azimuth direction is given as [Elachi and Van Zyl, 2006]

$$\Delta x = \frac{h\lambda}{D_a cos\theta} \, , \tag{3.4}$$

where h is the height above the ground, λ the wavelength, θ the incidence angle, and D_a the antenna length.

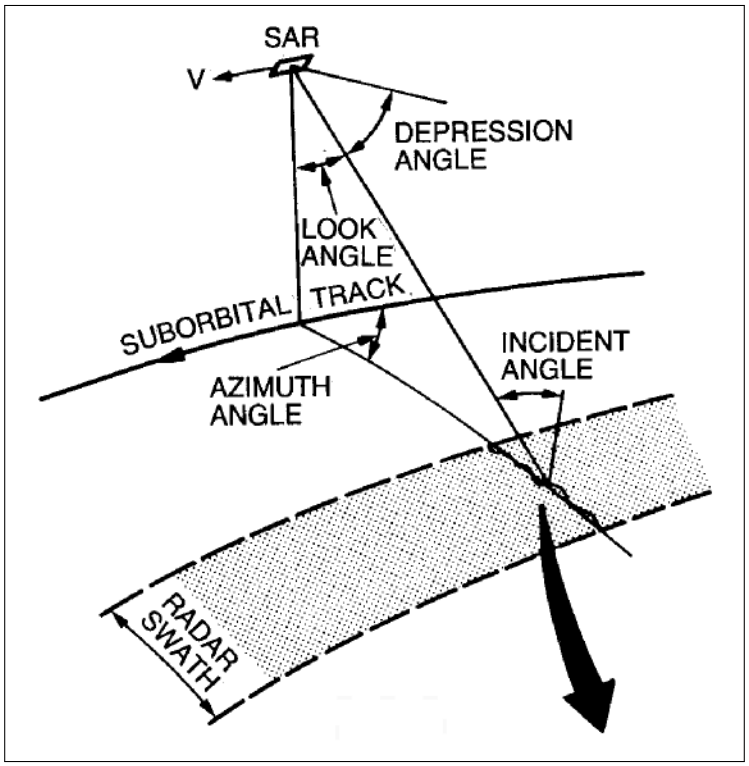

(a) Illustration of the radar geometry [Henderson et al., 1998].

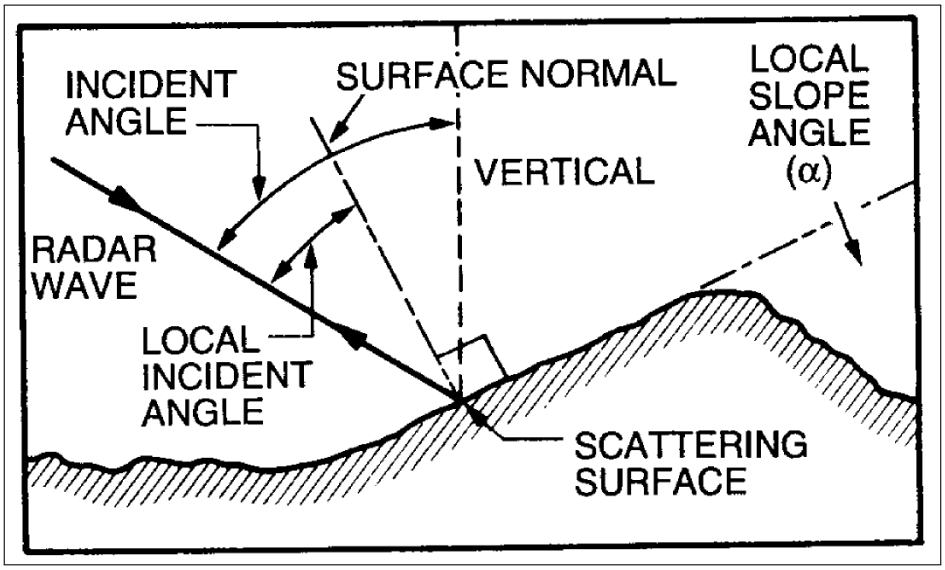

(b) Illustration of the geometry at the scattering surface, showing the difference between radar incident and local incident angles [Henderson et al., 1998].

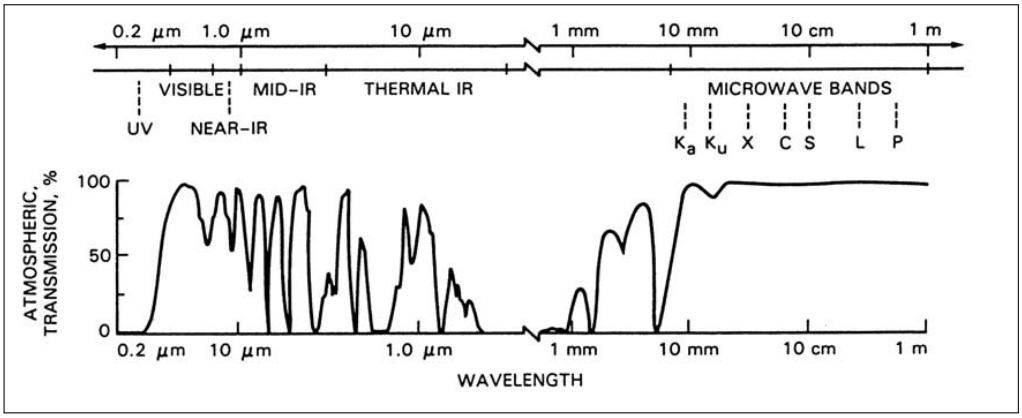

Figure 3.2: Overview over the atmospheric windows in the EM-spectrum that are used for remote sensing operations [Henderson et al., 1998].

The problem of RAR is that the resolution in azimuth direction is proportional to the distance from the target, which in satellite imaging is very large. One way to solve the problem is to increase the antenna length, which is what Synthetic Aperture Radars (SARs) do. They synthesize the antenna during post-processing to artificially simulate that the antenna is longer than it actually is using the Doppler history of the received signals. This allows for the following range resolution [Elachi and Van Zyl, 2006]

$$\Delta R = \frac{c}{2B_w} , \tag{3.5}$$

where B_w is the bandwidth and c the speed of light. The azimuth resolution is

$$\Delta x = \frac{D_A}{2} , \tag{3.6}$$

where D_a is the synthesized antenna length.

3.1.4 Frequency

The EM spectrum region of operation for radars is the microwave region with wavelengths from 1 mm to 100 cm (0.3 GHz - 300 GHz frequency). The microwave region is further divided into small bands as seen in Figure 3.2, where the Ka-, K-, and Ku-band cover the small wavelengths in the range between 0.75 and 2.4 cm. These bands are not applied from satellites due to the high atmospheric influence for those wavelength. The larger bands in the spectrum such as the X, C, S, L, and P bands range from 2.4 cm to 100 cm [Chuvieco et al., 2009].

Frequency or wavelength is a very important parameter in imaging, since it defines how the waves interact with the atmosphere. It, as previously discussed, also has an impact on the penetration depth and on the size that objects have to have to be distinguishable. For the major part of the microwave spectrum, the atmospheric effects are almost negligible.

As mentioned earlier, the quantity of interest in a radar system is the intensity of the return signal. This signal, however, is affected considerably by the roughness of the surface and generally a higher roughness results in greater backscatter. Roughness is a quantity that is dependent on the wavelength and the incidence angle, since roughness is usually considered as variation in surface height [Chuvieco et al., 2009]. A criterion often used to determine roughness is the Rayleigh criterion, which states that a surface is rough when

$$s_h \geq \frac{\lambda}{8} cos(\theta), \tag{3.7}$$

where s_h denotes the standard deviation of the surface height, θ the incidence angle and λ the wavelength. This means, that a surface looks smoother when illuminated with larger wavelengths or greater incidence angle than the identical surface would look with smaller wavelength or smaller incidence angle.

3.1.5 Polarization

SAR and RAR both make use of plane linear polarization [Chuvieco et al., 2009]. Initially, most radar systems transmitted waves at either horizontal or vertical polarization and received either horizontal or vertical polarization. However, in more recent years, advances have been made that allow antennas to transmit waves at different polarizations by switching in-between each pulse. Since antennas are able to receive both the vertical as well as the horizontal polarization waves simultaneously it is possible to record the following channels:

- Transmit and receive horizontal (HH)
- Transmit and receive vertical (VV)
- Transmit horizontal and receive vertical (HV)
- Transmit vertical and receive horizontal (VH)

where the first two are usually referred to as like-polarized, or co-polarized, and the last two as cross-polarized.

Modern radar systems can be divided into three main polarization groups. The first one being single polarized, which theoretically includes any single one of the bands mentioned previously. For practical reasons, however, the co-polarized bands are usually the only ones being used. There is also a group of dual polarized satellites that use the following bands (VV and VH, HH and HV, or HH and VV) and which comprises the second group. The last group consists of the systems that have all four polarizations and therefore provide the user with all of the four above mentioned bands. This last group is usually referred to as fully polarimetric or quad-polarization [Oliver and Quegan, 2004].

3.2 SAR measurements of sea ice

The previous section focused on the general geometry as well as the SAR sensor properties. This section instead focuses on the surface properties that affect the radar image.

3.2.1 Scattering mechanisms

Scattering, unlike specular reflections, is a physical process where radiation is dispersed in unpredictable directions [Jensen, 2009]. The three main types of scattering are surface scattering (single bounce), double bounce and volume scattering. They depend on the dielectric properties of the medium as well as the surface roughness, which is a quantity that depends on the wavelength, but most importantly on the local geometry. Sensor and geometric properties such as the frequency and the incident angle also play a role. Figure 3.3 illustrates the principles of single and double bounce as well as volume scattering using an example of snow on first year sea ice. Each of the previously mentioned scattering types is explained below.

Surface scattering - Single bounce

Single bounce scattering (in Figure 3.3 denoted as A) is a term used to describe reflections that have been dispersed only once by the surface boundary between two media. This occurs mainly on reasonably flat surfaces. There are three main types of surface scattering scenarios, which are illustrated in Figure 3.4. For very smooth surfaces, such as displayed in part a) of the Figure, the incident radiation is reflected perfectly, thus having a delta function as a radiation pattern for the reflected wave. Slightly rough surfaces as shown in part b) of the Figure cause the resulting radiation pattern to consist of two components. One is the reflected component, which is in the same direction

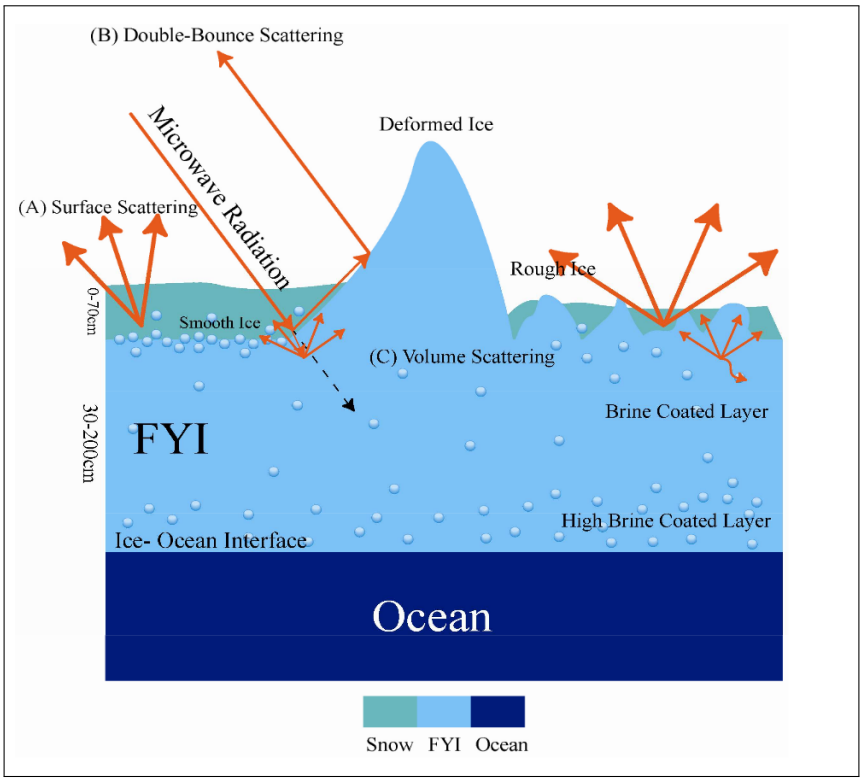

Figure 3.3: Scattering mechanisms for first year sea ice. Illustrating single bounce (A), double bounce (B) and volume scattering (C) [Hossain et al., 2012].

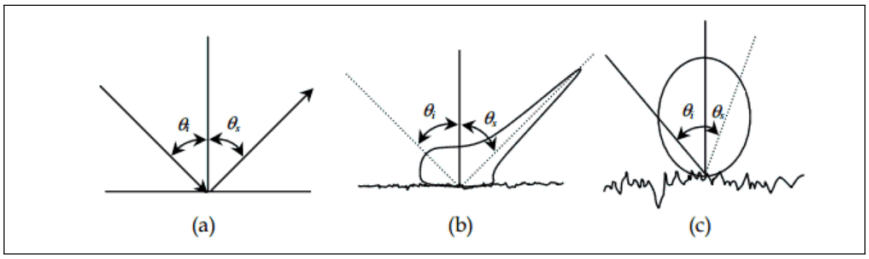

Figure 3.4: Surface scattering scenarios. Illustrating scattering for a smooth surface (a), a slightly rough surface (b) and a very rough surface (c) [Hossain et al., 2012].

as one would expect for the specular case, its magnitude, however, is not as large. The second component is the scattered component, which consists of the diffuse radiation that is scattered in all directions. The scattered components magnitude for slightly rough surfaces is lower than the reflected component [Hossain et al., 2012]. Very rough surfaces as illustrated in part c) of Figure 3.4, also referred to as Lambertian surfaces, are considered to be perfectly diffuse. This means that the reflected radiant intensity of the surface is independent of the viewing angle [Chuvieco et al., 2009].

Double bounce

Double bounce scattering refers to dihedral corner reflectors [Yamaguchi et al., 2005], where pulses are scattered twice, as displayed in Figure 3.3. Examples for corner reflectors can be deformed ice, as seen in Figure 3.3, or water/ice edges.

Volume scattering

Volume scattering is a different form of scattering that refers to the scattering inside the medium when pulses are transmitted from one medium to another, or inside a medium due to non-homogeneous material. Typical examples for volume scattering in sea ice include scattering due to inhomogeneities such as brine pockets, as can be seen in Figure 3.3, and also scattering by ice ridges. Snow layers on top of the sea ice are another scenario that can lead to volume scattering [Hossain et al., 2012]. Tree canopy is a common, non-ice example that can cause volume scattering [Freeman and Durden, 1998].

3.2.2 Radar cross section

As mentioned in section 3.1.1 the radar cross section is an important component of the radar equation, as it describes the ratio of the energy density that is scattered by the surface into the direction of interest to the incident energy density on the surface. Monostatic satellites record the energy that is scattered back to the satellite and image intensities in images produced by the SAR satellite are proportional to the ratio of the incoming energy density and the density of the scattered energy. The term backscatter coefficient that is often used in SAR imaging refers to

$$\sigma^0 = \frac{\sigma}{A}\,, \tag{3.8}$$

where σ is the radar cross section and A is the area on the ground. Due to the large variations in backscatter magnitude it is commonly expressed using decibels.

3.2.3 Dielectric properties

The electrical properties of the target have an important impact on the backscatter coefficient and thereby the intensity of the image in radar remote sensing. The complex dielectric constant has the most direct effect on the aforementioned backscatter coefficient by describing the ability of a medium to store and transmit electrons [Chuvieco et al., 2009]. It is commonly interchangeably used with the complex permittivity (section 2.3). Due to the large dielectric constant of water (≈ 80), the moisture of a material can have a large effect on backscatter.

4

Numerical modeling

This chapter focuses on the numerical model that has been implemented as part of the thesis. Section 4.1 provides a short overview of finite element modeling as well as the concepts that the model is based on. Section 4.2 describes the model that has been implemented and discusses certain simplifications that had to be made.

4.1 Finite element modeling background

Finite Element Method (FEM) is a numerical discretization technique for finding approximate solutions to Partial Differential Equations (PDEs) by dividing the continuous modeling domain up into disjoint sub-domains of simple geometry. It is widely used in physical modeling problems. Inside these sub-domains, referred to as finite elements or just elements, interpolation functions with a finite number of degrees of freedoms are used to represent the unknown functions. This reduces the number of degrees of freedom from infinitely many for the continuous solution to a finite number, thus making it possible to approximate the whole system from a finite set of coefficients. The solution to the entire problem is then approximated by assembling together all the element equations to a global finite element equation [Quek and Liu, 2003].

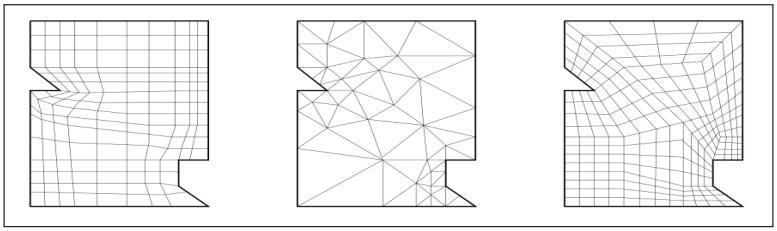

Figure 4.1: Meshing categories: Structured, unstructured and hybrid (left to right) [Bern and Plassmann, 1997].

4.1.1 Mesh generation

The mesh is the pattern that divides up the model domain into a set of small disjoint finite elements of simple geometry. The size of these elements is very important, since a mesh that is chosen to be too dense will require more computational resources than is necessary, whereas a mesh that is to sparse might cause the solution not to converge or will yield large approximation errors. The FEM allows the size of these elements to vary across the modeling domain and it is therefore possible to reduce the element size around interfaces or complex structures to achieve high accuracy and resolution.

The error of the approximate solution depends, however, not only on the size of the finite elements, but also on the position of the elements, which is why the mesh generation process is important [Lo, 2002]. The three main categories of mesh generation methods are structured, unstructured meshing, and hybrid (also called block-structured) meshing. They are illustrated in Figure 4.1. All these methods have both advantages and disadvantages. The structured mesh, for example, benefits from the simplicity, while the unstructured mesh is more suitable for complex domains by offering better mesh adaptivity. Hybrid meshing combines the advantages of both methods by combining small structured meshes in a large unstructured mesh. It has, however, the disadvantage of being difficult to generate fully automatically [Bern and Plassmann, 1997].

In this thesis, the meshing has been performed using unstructured triangular meshes to allow the meshing of complex structures such as the rough surface (see example domain geometry in Figure 5.16).

4.1.2 Wave equation

The propagation of electromagnetic waves through a medium is a simple problem in electromagnetics and can be solved with the help of Maxwell's equations, which are specified in [Lillestøl et al., 2001] as

$$\nabla \cdot \boldsymbol{D} = \rho \tag{4.1}$$

$$\nabla \times \boldsymbol{E} = -\frac{\partial \boldsymbol{B}}{\partial t} \tag{4.2}$$

$$\nabla \times \boldsymbol{H} = \boldsymbol{J} + \frac{\partial \boldsymbol{D}}{\partial t} \tag{4.3}$$

$$\nabla \cdot \boldsymbol{B} = 0 \,, \tag{4.4}$$

where **E** denotes to the electric field, **B** the magnetic field, **D** is the displacement field, **H** is the magnetizing field, **J** the free electric current density, and ρ is the free charge density.

In addition to these, the following relations

$$\boldsymbol{D} = \epsilon \boldsymbol{E} = \kappa \epsilon_0 \boldsymbol{E} \tag{4.5}$$

$$\boldsymbol{B} = \mu \boldsymbol{H} = \mu_r \mu_0 \boldsymbol{H} \tag{4.6}$$

are valid for materials that are both linear and isotropic [Lorrain and Corson, 1970], where ϵ is the permittivity of the medium, ϵ_0 the permittivity of free space, μ the permeability of the medium, μ_r the relative permeability, μ_0 the permeability of free space, and κ the dielectric constant. The governing equation that needs to be solved can be derived by combining Maxwell's equation and the material equations, equations (4.5) and (4.6), with Ohm's law

$$\boldsymbol{J} = \sigma_c \boldsymbol{E} \tag{4.7}$$

and the fact that the waves in our model are planar waves of form

$$\boldsymbol{E}(\boldsymbol{r}, t) = \boldsymbol{E}(\boldsymbol{r}) e^{j\omega t} \,, \tag{4.8}$$

where σ_c is the electrical conductivity and ω is the angular frequency of the wave. The governing equation is

$$\nabla \times \mu_r^{-1}(\nabla \times \boldsymbol{E}) - k_0^2(\epsilon_r - \frac{j\sigma_c}{\omega \epsilon_0}) = 0 \,, \tag{4.9}$$

where k_0 is the wave number in vacuum, which is defined as

$$k_0 = \omega \sqrt{\epsilon_0 \mu_0} = \frac{\omega}{c} \,, \tag{4.10}$$

where c is the speed of light in vacuum [Jin et al., 2002].

4.1.3 Boundary conditions

Equation 4.9 in the previous section has many functions that satisfy it and it is necessary to consider the boundary conditions of the domain to find the single real solution of the problem. These boundary conditions, which are the relationships that the electric and magnetic field components have to comply to at interfaces between different materials, can be derived from Maxwell's equation.

At the interface between two media

$$\boldsymbol{n} \times (\boldsymbol{E_1} - \boldsymbol{E_2}) = 0 \tag{4.11}$$
$$\boldsymbol{n} \times (\boldsymbol{H_1} - \boldsymbol{H_2}) = 0 \tag{4.12}$$
$$\boldsymbol{n} \cdot (\boldsymbol{D_1} - \boldsymbol{D_2}) = 0 \tag{4.13}$$
$$\boldsymbol{n} \cdot (\boldsymbol{B_1} - \boldsymbol{B_2}) = 0 \tag{4.14}$$

need to be satisfied as long as no surface currents or surface charges exists. Here $\boldsymbol{n}$ is the unit vector normal to the interface and $\mathbf{B}$, $\mathbf{E}$, $\mathbf{D}$, and $\mathbf{H}$ are the magnetic, displacement, electric and the magnetizing field respectively with the index indicating medium 1 and medium 2 [Jin et al., 2002]. This means that the tangential component of both the electric field as well as the magnetic field is continuous across interfaces.

If, however, surface currents or surface charges exist, the boundary conditions will be

$$\boldsymbol{n} \cdot (\boldsymbol{D_1} - \boldsymbol{D_2}) = \rho_s \tag{4.15}$$
$$\boldsymbol{n} \times (\boldsymbol{H_1} - \boldsymbol{H_2}) = \boldsymbol{J_s}\ , \tag{4.16}$$

where ρ_s is the surface charge and $\mathbf{J_s}$ is the surface current.

For imperfect conductors, the impedance boundary condition can be written as

$$\frac{1}{\mu_{r1}} \boldsymbol{n} \times (\nabla \times \boldsymbol{E}) - \frac{jk_0}{\eta} \boldsymbol{n} \times (\boldsymbol{n} \times \boldsymbol{E}) = 0 \tag{4.17}$$
$$\frac{1}{\epsilon_{r1}} \boldsymbol{n} \times (\nabla \times \boldsymbol{H}) - jk_0 \eta \boldsymbol{n} \times (\boldsymbol{n} \times \boldsymbol{H}) = 0, \tag{4.18}$$

where $\eta = \sqrt{\frac{\mu_{r2}}{\epsilon_{r2}}}$ is the normalized intrinsic impedance, and k_0 is the wavenumber in free space for the case where medium 2 is the imperfect conductor [Jin et al., 2002].

Another type of boundary that is often used to act as an exterior boundary of the model is the perfectly conducting surface. The boundary condition of a perfect conductor is

$$\boldsymbol{n} \times \boldsymbol{E} = 0 \tag{4.19}$$
$$\boldsymbol{n} \times \boldsymbol{H} = 0 \tag{4.20}$$

since they can not sustain internal fields.

Periodic boundary conditions

It is often helpful to model a domain (or surface) with infinite extent, for example, to be able to compare a result with a theoretical solution. One way to do this would be to make the model very large to reduce the effect of the boundaries, which would, however, use large amounts of computer resources and is therefore not a reasonable way to do it. The other way this can be done is to make use of Periodic Boundary Conditions (PBC), which can overcome the problem, as long as the surface is periodic, by replicating the surface to form an infinite surface.

One example of a PBC, which is commonly used to model plane waves that interact with periodic structures, is the Flouquet boundary condition. It accounts for the phase shift between points in the different unit cells of the infinite structure [Collin, 2001], by making use of the wave vector and the distance between the source (src) and destination (dst) point, such that

$$\boldsymbol{E}_{dst} = \boldsymbol{E}_{src} e^{-i\boldsymbol{k}_F \cdot (\boldsymbol{r}_{dst} - \boldsymbol{r}\,src)} \tag{4.21}$$
$$\boldsymbol{H}_{dst} = \boldsymbol{H}_{src} e^{-i\boldsymbol{k}_F \cdot (\boldsymbol{r}_{dst} - \boldsymbol{r}\,src)}, \tag{4.22}$$

where $\mathbf{k_F}$ is the wave vector for Floquet periodicity and $\boldsymbol{r}_{dst} - \boldsymbol{r}_{src}$ is the distance between the two points.

4.1.4 Boundary value problems

A boundary-value problem is the problem of solving the differential equation in a certain domain, whilst satisfying the boundary conditions. Solving these problems analytically is rarely possible, and in practice most problems do not have an analytical solution. Solving these problems is the fundamental basis of FEM [Jin et al., 2002] and is mathematically expressed as a differential equation in domain Ω of type

$$\mathcal{L}\phi = f_f \ , \tag{4.23}$$

where $\mathscr{L}$ is the differential operator, f_f the forcing function and ϕ the unknown quantity, combined with a boundary condition enclosing the domain Ω.

One of the main methods classically used to solve the Partial Differential Equation (PDE) problem is the Ritz variational method (also called the Rayleigh-Ritz method), which is shortly described in the next section.

The Ritz Method

The Ritz method belongs to the group of variational methods and formulates the systems of equations to solve the boundary-value problem as a function of functions, a functional, whose minimum is the differential equation restricted by the given boundary conditions [Jin et al., 2002].

The advantage of this method compared to the Galerkin's method, another method commonly used in numerical modeling, is that it often allows for a more elegant formulation of the problem and for easier interpretation in regards to the physics involved.

Most boundary values problems in electromagnetics can be formulated using the general variational principle [Jin et al., 2002], which allows the formulation of lossy media (the complex permittivity) or other complex quantities as well as inhomogeneous boundary conditions. To support inhomogeneous boundary conditions a new unknown function $\phi' = \phi - u$ is introduced, in an effort to make the problem self-adjoint, by letting ϕ' satisfy homogeneous boundary conditions. The old problem in equation 4.23 can therefore be redefined to allow inhomogeneous boundary conditions, which results in the expression

$$\mathscr{L}\phi' = f_f' \ . \tag{4.24}$$

The functional F for such scenarios is given as

$$F(\phi) = \frac{1}{2}\langle \mathscr{L}\phi, \phi \rangle - \frac{1}{2}\langle \mathscr{L}\phi, u \rangle + \frac{1}{2}\langle \phi, \mathscr{L}u \rangle - \langle \phi, f_f \rangle \ , \tag{4.25}$$

where the inner product is defined as

$$\langle \phi, \psi \rangle = \int_{\Omega} -\phi\psi d\Omega \ . \tag{4.26}$$

With this definition, the electromagnetic boundary value problem for the wave equation can be found. Combining the wave equation with

$$\frac{1}{\mu_{r1}} \boldsymbol{n} \times (\nabla \times \boldsymbol{E}) + \gamma_e \boldsymbol{n} \times (\boldsymbol{n} \times \boldsymbol{E}) = \boldsymbol{U} \ , \tag{4.27}$$

which is a more generalized version of the boundary condition that was specified in equation 4.17 and which can be used to represent impedance boundary conditions as well as the Sommerfeld radiation condition. This allows the electromagnetic boundary value to be expressed as

$$\begin{aligned} F(\boldsymbol{E}) = \frac{1}{2} \iiint_V \left[\frac{1}{\mu_r} (\nabla \times \boldsymbol{E}) \cdot (\nabla \times \boldsymbol{E}) - k_0^2 \epsilon_r \boldsymbol{E} \cdot \boldsymbol{E} \right] dV \\ + \iint_{S_2} \left[\frac{\gamma_e}{2} (\boldsymbol{n} \times \boldsymbol{E}) \cdot (\boldsymbol{n} \times \boldsymbol{E}) + \boldsymbol{E} \cdot \boldsymbol{U} \right] dS \\ + jk_0 Z_0 \iiint_V \boldsymbol{E} \cdot \boldsymbol{J} dV \ , \end{aligned} \tag{4.28}$$

where Z_0 is the intrinsic impedance of free space given as $\sqrt{\frac{\mu_0}{\epsilon_0}}$, γ_e is a known parameter that for impedance boundary conditions will be $-\frac{jk_0}{\eta}$ and $\boldsymbol{U}$ is a known vector that can be used to represent the boundary condition [Jin et al., 2002].

4.1.5 Perfectly Matched Layers

A Perfectly Matched Layer (PML) is a technique that allows the simulation of infinite unbounded domains in electromagnetics, and was proposed in [Berenger, 1994]. Open boundaries often represent a problem, since it is in many problems impossible to accurately define the direction of the outgoing radiation as a plane wave or the direction of propagation [COMSOL, 2012]. PMLs are nonphysical anisotropic materials that are meant to absorb uniform plane waves at any incidence angle, any frequency and any polarization without reflection.

This is achieved by adding degrees of freedom to Maxwell's equations by including a complex-valued coordinate transformation and by allowing the wave impedance not to change [Jin et al., 2002]. In practice, this is not exactly true in a numerical analysis due to discretization, which still leads to some reflections [Peterson et al., 1998]. Using a PML does, however, reduce these to a minimum, so that they should not effect simulation results considerably.

Various interpretations, generalizations, and improvements of the original PML exist. One of these [Chew and Weedon, 1994] is based on a coordinate stretching approach, where the Cartesian coordinates are stretched by the factors s_x,s_y and s_z along their respective axis. The reader is referred to the paper for more information as well as the rigorous proof.

4.1.6 Far field

The electromagnetic field around a scatterer object or an antenna can be divided up into a near field and a far field as illustrated in Figure 4.2. The border between the two fields is dictated by the Fraunhofer (or Far field) distance, which is

$$d_f = \frac{2D_a^2}{\lambda} , \tag{4.29}$$

where D_a is the aperture dimension of the antenna or the period of the scatterer, and λ is the wavelength [Stutzman and Thiele, 2012].

Whereas the near field does generally have a field pattern that can differ considerable from one point to another and that is generally quite complicated, the field pattern for the far field is usually simpler and more predictable as it approaches a plane wave pattern. The near field can be divided up further into the reactive near field and the radiating near field as seen in Figure 4.2, where the reactive fields dominate the radiation fields and the radiation fields dominate the reactive fields, respectively.

An equation that is commonly used to calculate the far field from the near field is the Stratton-Chu equation [Stratton, 2007], which in two dimensions is given as

$$\boldsymbol{E}_p = \sqrt{\lambda}\frac{jk}{4\pi}\boldsymbol{r}_0 \times \int [\boldsymbol{n} \times \boldsymbol{E} - \eta \boldsymbol{r}_0 \times (\boldsymbol{n} \times \boldsymbol{H})] e^{jk\boldsymbol{r}\cdot\boldsymbol{r}_0} dS , \tag{4.30}$$

where **E** and **H** are the electric and magnetic fields on a surface S that encloses the scattering surface, $\boldsymbol{r}_0$ is the unit vector from the origin to the field point p, $\boldsymbol{n}$ is the unit normal from the surface S, λ the wavelength, k the wavenumber, $\boldsymbol{r}$ is

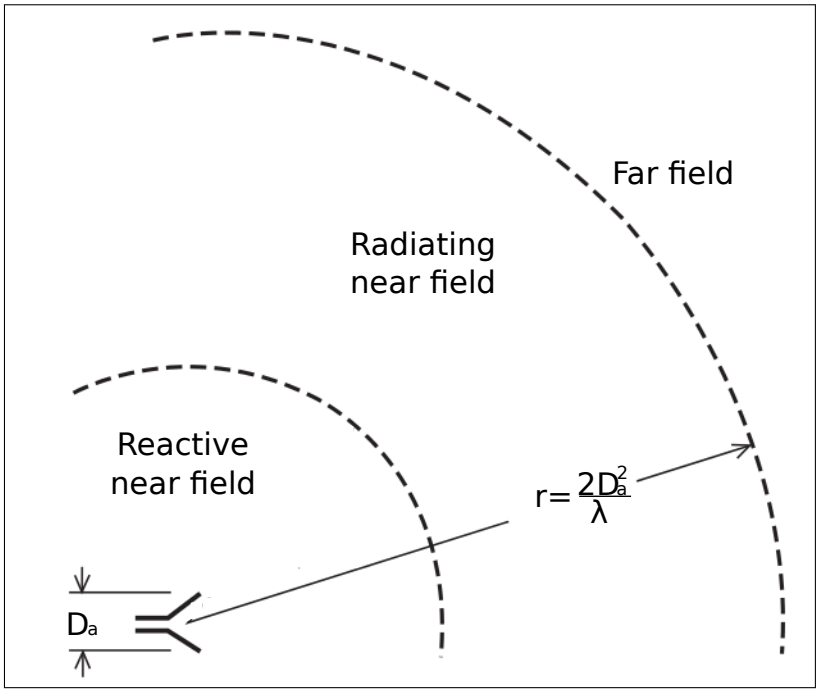

Figure 4.2: Electromagnetic field around an antenna/scatterer, showing the far and near field [Stutzman and Thiele, 2012].

the radius vector of S, and η the impedance, which is defined as $\sqrt{\frac{\mu}{\epsilon}}$ [COMSOL, 2012].

Assuming that the surface is located at the origin and point p in the far field is at infinity at an angular position (θ,ϕ), it is possible to interpret the unit vector $\boldsymbol{r}_0$ as the direction defined by (θ,ϕ), which means that $\mathbf{E_p}$ will be the far field in that direction.

The far field radiation pattern can be expressed as $|E_p|^2$ [COMSOL, 2012].

4.1.7 Radar cross section

An important parameter for open region scattering problems as well as in the case of SAR imaging is the radar cross section (as described in section 3.2.2).

It can be found as

$$\sigma(\theta^{sc},\phi^{sc},\theta,\phi) = \lim_{r\to\infty} 4\pi r^2 \frac{|\boldsymbol{E^{sc}}(r,\theta^{sc},\phi^{sc})|^2}{|\boldsymbol{E^{inc}}(\theta,\phi)|^2}\ , \tag{4.31}$$

where $\mathbf{E^{inc}}$ and $\mathbf{E^{sc}}$ are the incident field from direction (θ,ϕ), and the scattered field in the direction (θ^{sc},ϕ^{sc}), respectively [Jin et al., 2002]. The scattered field can be found using equation (4.30).

As previously stated in section 3.2.2, the radar cross section is referred to as the backscattering cross section when the incident direction is the same as the observation direction. In the context of equation (4.31), this means $(\theta,\phi) = (\theta^{sc},\phi^{sc})$. The radar cross section is usually normalized by the surface area that is illuminated to yield the backscatter coefficient.

4.1.8 COMSOL

COMSOL Multiphysics 4.4 was used as modeling software. It originates from MATLABs PDE toolbox, which could solve classical equations in 2D. Over time, the functionality was extended to support 3D scenarios and was called Femlab. In 2005 Femlab was renamed to COMSOL Multiphysics and is no longer reliant on MATLAB. It is, however, still fully compatible with MATLAB, which allows users to incorporate their models into MATLAB scripts.

Stallo

As part of this project, the supercomputer Stallo at the University of Tromsø – Norges arktiske universitet had to be used to cope with the amount of computational resources needed to model the domain. Initially the model was developed and run on the server of the remote sensing group at the University (2x2.93GHz Quad-Core Intel Xeon, 32GB Memory). This worked fine when working with small models or large wavelengths, but it was soon apparent that more memory was required to solve larger models in C-Band, making the move to Stallo necessary. The move to Stallo offered an increased amount of resources but did in return also introduced the variable of a queuing system where, depending on the load of Stallo, jobs occasionally had to wait up to 3 days in a queue. Table 4.1 shows the specifications of Stallo.

A typical version of the pixel sized model ($4m$ extent), which can be seen in section 5.3, run on Stallo has the requirements shown in Table 4.2. It can be seen, that even models representing one pixel in size require large amounts of computation, making it impractical/impossible to model a whole radar image in one go. It was not considered to decrease the modeling domain even further since that would complicate the comparison to remote sensing scenarios considerably.

Table 4.1: Stallo resource description from the Stallo user guide [Notur, 2013]

	Aggregated	Per Node
Peak performance	201 Teraflop/s	332 Gigaflop/s [a] 448 Gigaflop/s [b]
Total memory	19.7 TB	32 GB (32 nodes with 128 GB)
Internal storage	155.2 TB	500 GB (32 nodes with 600GB raid)
Centralized storage	2000 TB	

[a] For the 304 HP BL460 gen8 blade servers
[b] For the 216 HP SL230 gen8 servers

Table 4.2: Requirements for a typical COMSOL job for the geometry in section 5.3

Boundary elements	26 186
Total elements	5 670 586
Number of degrees of freedom	39 704 223
Number of nodes	10
Solution time	4h,17min,22sec

4.2 Model design and simplifications

This section focuses on the model that was designed using the COMSOL Multiphysics RF Module. It explains the key design choices that were made during the process and mentions certain simplifications that had to be made to the model. Some fieldwork is included into the design of the model, which is described in section 4.2.1. Section 4.2.2 discusses the Fresnel equations for multilayer structures, which have been used to validate the model.

4.2.1 Fieldwork: Complex Permittivity

To make the model as realistic as possible, valid input parameters were required, which is why some fieldwork data has been included. As part of a research cruise in the Svalbard area, the temperature, density, and salinity of first year sea ice was measured at the entrance of Van Keulenfjord towards the end of April 2011 using the method described in section 2.1.4. The temperature was measured using a thermistor thermometer with an accuracy of ±0.2°C and a resolution of 0.1°C. The measurements were taken in small drilled holes in the core prior to cutting the core up into smaller sections. The small sections were then placed on a small tray to minimize the effect of the surroundings and were measured using a trammel before weighing them with a weight scale with a accuracy

of $\pm 3g$ and a resolution of $1g$. The samples were then placed in bags and set to melt.The salinity was measured once the samples were completely melted using a salinity meter with an accuracy of $\pm 0.01ppt$ and a resolution of $0.01ppt$. The salinity meter was calibrated using the calibration solution that followed with the instrument. Even though the method is relatively easy to perform, additional sources of errors for both salinity and density can, for example, be introduced by sample drainage caused by exposure to air temperatures.

An example of one of the recorded salinity profiles, temperature profiles, and density profiles is shown in Figures 4.3, 4.4 and 4.5 respectively. Figure 4.3 shows the distinct C-shape curve discussed in section 2.1.3 and similarities to the June profile in Figure 2.1 can clearly be seen. At the end of April, the air temperature was already high enough to cause melt water flushing in the top layer, which explains the low surface salinity. It also explains the temperature profile in Figure 4.4, where the top part of the ice has been warmed by the air temperature and the bottom by the sea water, causing the temperature, which during the winter increased with depth, to be lower in the middle of the block.

By using the data to calculate the relative brine volume using the equations described in section 2.1.4 and combining the result with the model discussed in section 2.3.1, it was possible to calculate an approximate distribution of the permittivity with depth. In the calculation, the depolarization factors A_u of the inclusion were chosen to represent oriented needles to fit the inclusion geometry that can be expected in well-developed first year sea ice [Shokr, 1998]. The frequency was chosen as 5.405GHz to fit the models discussed in chapter 5, which use the permittivity profile. Figure 4.6a and 4.6b show the permittivity profiles that were generated and refer to the real and imaginary part, respectively.

It is important to note that the data used includes only in situ TDS measurements and that these can vary significantly over the area of a whole image. Since, however, only one image pixels was modeled it is an reasonable assumption that the measurements over the area of the pixel should not differ considerably.

4.2.2 Fresnel equation

An important part of designing a model is to validate it by comparing it to an analytical solution (if available), or to other models or experimental results. There exists an analytical solution for the case that is being considered in section 5.1, which models a two layered medium with a perfectly flat surface. The analytical solution to this problem can be found by making use of the

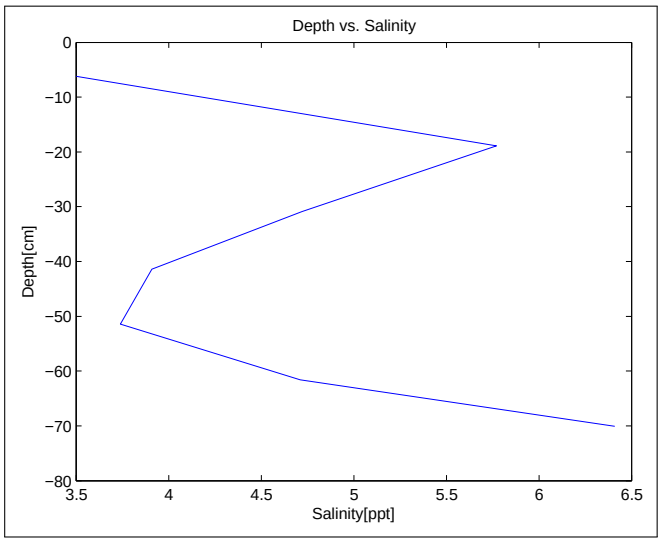

Figure 4.3: Salinity-depth profile of one of the cores taken in Van Keulenfjord.

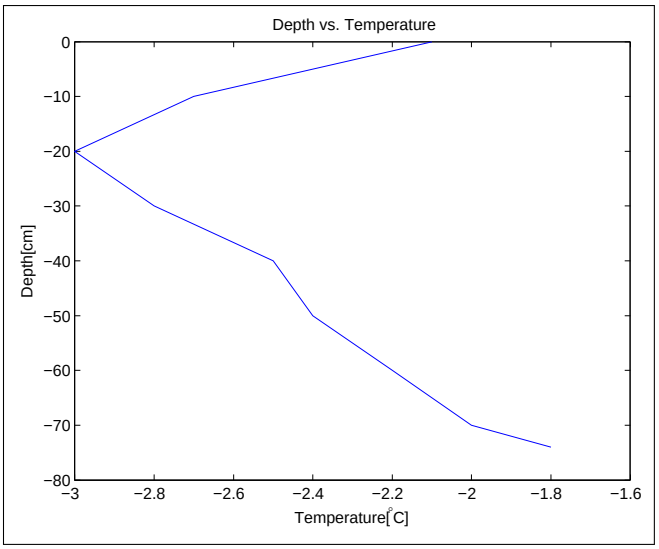

Figure 4.4: Temperature-depth profile of one of the cores taken in Van Keulenfjord.

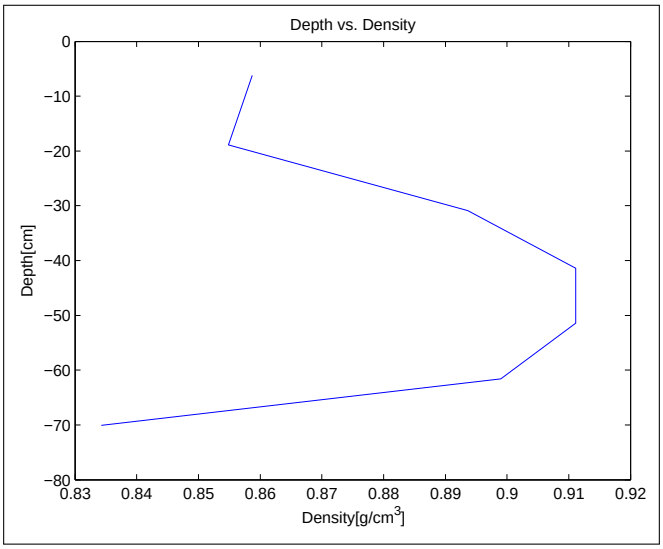

Figure 4.5: Density-depth profile of one of the cores taken in Van Keulenfjord.

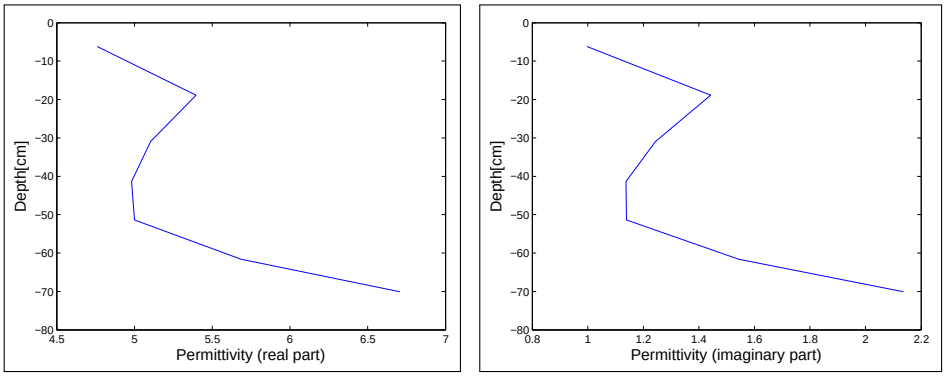

(a) Real part **(b)** Imaginary part

Figure 4.6: Permittivity-depth profile of one of the cores taken in Van Keulenfjord. The model described in section 2.3.1 was used to generate the profile.

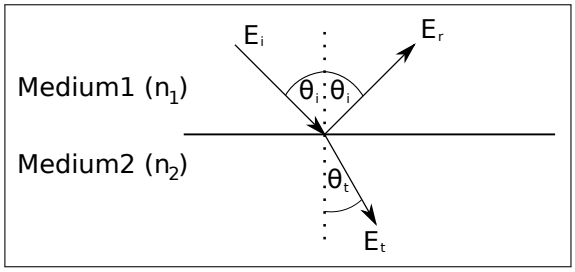

Figure 4.7: Illustrates the incidence, transmitted and reflected part of the **E**-field for the boundary between two media with refractive index n_1 and n_2. The incidence angle for the surface is denoted θ_1 and the angle of transmission is denoted with θ_2.

Fresnel equations, which are given as

$$r_s = \frac{n_1 cos\theta_i - n_2 cos\theta_t}{n_1 cos\theta_i + n_2 cos\theta_t} \tag{4.32}$$

$$t_s = \frac{2n_1 cos\theta_i}{n_1 cos\theta_i + n_2 cos\theta_t} \tag{4.33}$$

$$r_p = \frac{n_2 cos\theta_i - n_1 cos\theta_t}{n_1 cos\theta_t + n_2 cos\theta_i} \tag{4.34}$$

$$t_p = \frac{2n_1 cos\theta_i}{n_1 cos\theta_t + n_2 cos\theta_i} \tag{4.35}$$

for the boundary between two mediums with refractive indices n_1 and n_2 (see Figure 4.7) [Bohren and Huffman, 1998]. In the above equation θ_i and θ_t refer to the angle of incidence and the angle of transmission, while r_s, t_s, r_p, and t_p are the reflection coefficient and the transmission coefficient for s-polarized wave and the reflection coefficient and the transmission coefficient for p-polarized wave, respectively.

When considering a three layer geometry as displayed in Figure 4.8 the total reflection can be found as

$$r_x = \frac{r_{12x} + e^{2j(n_2 k)dcos(\theta_2)} r_{23x}}{1 + e^{2j(n_2 k)dcos(\theta_2)} r_{12x} r_{23x}}\ , \tag{4.36}$$

where r_{12x} and r_{23x} are the reflection coefficient at the boundary between medium 1 and 2 and the boundary between medium 2 and 3 respectively, with x denoting either s- or p-polarization. d is the thickness of the second medium, k the wavenumber, n_2 the complex refractive index of medium 2, and θ_2 the angle at which the wave propagates in the second medium.The reader is referred to Appendix C for a detailed derivation of equation (4.36).

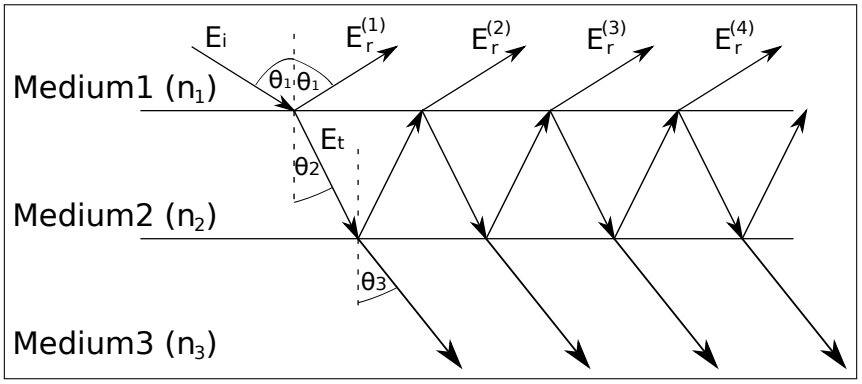

Figure 4.8: Displays the incidence, transmitted and reflected part of the **E**-field for the three layer structure. The incidence angle for the top surface is denoted θ_1, whereas the angle of incidence for the second surface is denoted with θ_2. The refractive indices are n_1,n_2 and n_3 (top to bottom).

Once the total reflection coefficient r_x has been found, the reflectance is

$$R = |r_x|^2 \ . \tag{4.37}$$

4.2.3 Random rough Gaussian surface generation

This section describes how a one-dimensional random rough surface is generated with a Gaussian correlation function and is based on the first two volumes of the Scattering of Electromagnetic Waves series [Tsang et al., 2000], [Tsang et al., 2001].

A random surface can be represented by a function defining the height of the surface. This can be defined as $z = f(x)$ where $f(x)$ has zero mean and is a random function of x. Assuming a stationary random process, it is known that

$$\langle f(x_1)f(x_2)\rangle = h^2 C(x_1 - x_2) \ , \tag{4.38}$$

where C is the correlation function and h the RMS height. For this thesis the correlation function of interest is the Gaussian

$$C(x) = e^{\frac{-x^2}{l^2}} \tag{4.39}$$

where l is the correlation length.

Equation (4.38) can be expressed using the spectral density as

$$h^2 C(x) = \int_{-\infty}^{\infty} dk_x e^{ik_x x} W(k_x) \,, \tag{4.40}$$

where the spectral density for the Gaussian correlation function (equation (4.39)) is

$$W(k_x) = \frac{h^2 l}{2\sqrt{\pi}} e^{-\frac{k_x^2 l^2}{4}} \,. \tag{4.41}$$

To generate a surface of length L the surface function $f(x)$ can be considered to have a period of length L, such that $f(x) = f(x + L)$. Such a function can be expressed as a fourier series

$$f(x) = \frac{1}{L} \sum_{n=-\infty}^{+\infty} b_n e^{\frac{i2\pi nx}{L}} \tag{4.42}$$

with the Gaussian random variable b_n, thus

$$\langle f(x_1) f(x_2) \rangle = \frac{1}{L^2} \sum_{n=-\infty}^{+\infty} \sum_{m=-\infty}^{+\infty} \langle b_n b_m^* \rangle e^{\frac{i2\pi nx_1}{L}} e^{\frac{-i2\pi mx_2}{L}} \,. \tag{4.43}$$

Comparing equation 4.40 and 4.38 with equation 4.43 and discretizing k_x at K_n where

$$K_n = \frac{2\pi n}{L} = n\Delta k_x \tag{4.44}$$

yields the following relations

$$\langle b_n b_m^* \rangle = \delta_{nm} B_n \tag{4.45}$$

and

$$\frac{2\pi}{L} \sum_{n=-\infty}^{\infty} e^{iK_n(x_1 - x_2)} W(K_n) = \frac{1}{L^2} \sum_{n=-\infty}^{\infty} B_n e^{iK_n(x_1 - x_2)} \,. \tag{4.46}$$

Equation (4.46) can be simplified to

$$B_n = 2\pi LW(K_n) \tag{4.47}$$

and combined with equation (4.45) can be written as

$$\langle |b_n|^2 \rangle = 2\pi LW(K_n) \ . \tag{4.48}$$

Since it is known that $f(x)$ is real the relation $F(K_n) = F^*(-K_n)$ is valid and since b_n and $F(K_n)$ are proportional to each other it can be implied that $b_n = b^*_{-n}$. Using this and setting $m = -n$ in equation (4.45) it can be shown that

$$\langle \Re(b_n) \rangle \langle \Im(b_n) \rangle = 0 \tag{4.49}$$

which means that the real and imaginary part of b_n are both independent Gaussian random variables.

Making use of the Discretized Fourier Transform (DFT) equation (4.42) can be expressed as

$$f_m = \frac{1}{L} \sum_{m=-\frac{N}{2}+1}^{\frac{N}{2}} b_n e^{i\frac{2\pi nm}{N}} \tag{4.50}$$

where $f(x_m) \equiv f_m$ and where the relations

$$\Delta x = \frac{L}{N} \ , \tag{4.51}$$

$$x_m = m\Delta x \ , \tag{4.52}$$

and

$$m = -\frac{N}{2} + 1, \ldots, 0, 1, \ldots, \frac{N}{2} \tag{4.53}$$

have been used to let there be N points in both the spacial and spectral domain.

Using the inverse DFT equation (4.50) can be used to express b_n as

$$b_n = \frac{L}{N} \sum_{m=-\frac{N}{2}+1}^{\frac{N}{2}} f_m e^{-i\frac{2\pi nm}{N}} \quad . \tag{4.54}$$

This allows the generation of the surface profile by first calculating all N b_n from a set of N random Gaussian distributed numbers and then using it to find f_m.

4.2.4 Material properties

In the model design phase, the decision was made to not represent the complex internal structure of the sea ice individually, but instead for simplicity to assume that the brine and air inclusions in the sea ice are on scales smaller than the wavelength. Taking experimental sizes into account, which were taken from [Perovich and Gow, 1996], this seems to be a reasonable assumption, as the mean area of a first year brine pocket was found to be $0.029mm^2$. For such small inclusions it is possible to replace the complex ice layer with a homogeneous material whose effective material properties will have the same effect as the complex structure. In the final part of the modeling, when including the field-work data, the effective permittivity (from measurements) was interpolated and used to have the material change its permittivity with depth. For multi year sea ice, however, the air inclusions are considerably larger than for first year ice and the assumption of homogeneity can not be utilized due to the fact that the large air inclusions will effect the volumetric scattering component.

4.2.5 Design decisions

During the development phase many problems were encountered, some related to the internal workings of COMSOL Multiphysics, and others related to computational issues such as described in section 4.1.8, which resulted in the necessity to reduce the modeling domain to the size that represents a pixel instead of a whole image. Another computational issue that had to be considered was the dimension of the model domain, which initially was chosen to be in 3 dimensions, but was reduced to 2 dimensions to avoid the meshing and solving of the extra dimension. This decision does, however, come at a cost, since it introduces some geometrical problems when trying to normalize the radar cross section by the area when the surface is being represented only by one dimension.

Another design decision that had to be made was on the mesh density. Here

the trade-off discussed in section 4.1.1 between limiting the discretization errors and limiting the complexity of the model was encountered. To limit the complexity it was chosen to follow the rule of thumb of using 6 elements per wavelength as discussed in [Marburg, 2002]. This was taken as the maximum element size, but towards the boundaries, especially the rough surface, the meshing density was dynamically increased using COMSOL functionality to reduce the discretization errors.

The author has also decided to avoid modeling the incident waves as chirps, and even the aperture synthesis, which are used in SAR to achieve high resolutions using post-processing, but has instead chosen to make use of planar waves, which corresponds more to a RAR sensor approach.

5

Results and Discussion

In this chapter, the different scenarios are described in more detail and the modeling results are presented and discussed. The first scenario that is considered and presented in section 5.1, is of a perfectly flat surface that, by using periodic boundary conditions, is simulated to be infinitely long. The second one is for a periodic surface that is limited in length (section 5.2). The model is compared to results from the SPM model in section 5.3, before a very rough surface is considered in section 5.4. The case described in section 5.5 presents a two layered rough surface model that makes use of the fieldwork measurements by including the permittivity profile found in section 4.2.1.

5.1 Case I: Two layered medium with plane surface and periodic boundary conditions simulating infinite extent

In this section a model is considered that consists of a 20 cm sea ice layer on top of a sea water layer. PBCs are used to let the domain represent a surface of infinite width.

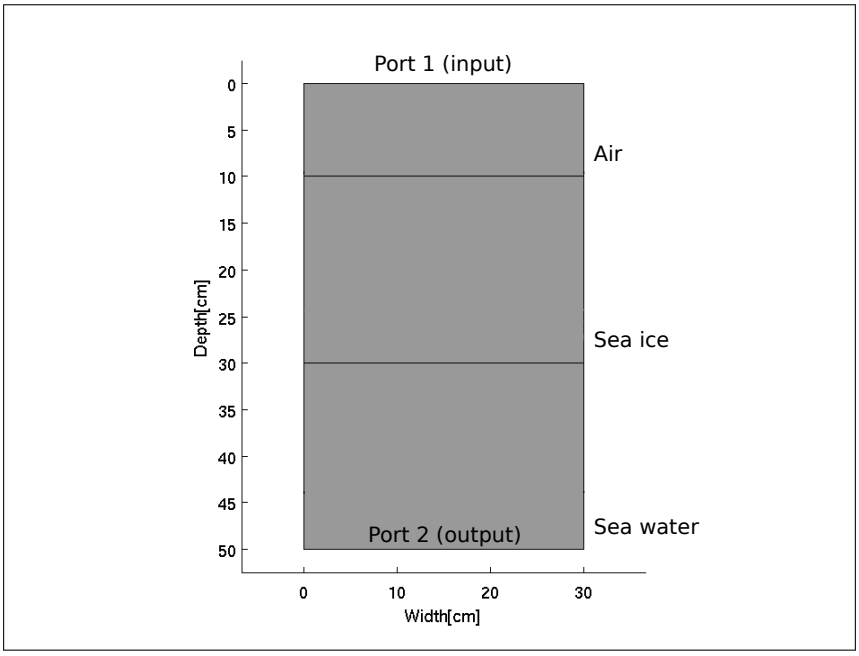

Figure 5.1: Case I: Planar surface model geometry.

5.1.1 Description

This model has been designed similar to the one proposed in [Yang and Altermatt, 2008], in which the reflectance of silicon solar cells has been modeled. The model geometry is presented in Figure 5.1, where the top side is defined as the input port, which is excited separately with a Transverse Electric (TE) wave and a Transverse Magnetic (TM) wave of the form discussed in section 4.1.2. The bottom side is the output port and has no excitation. The left and right side have been fitted with Floquet boundary conditions to ensure that waves that reach the edge are transposed to the other edge with the correct phase shift.

The three different media from top to bottom are air, sea ice and sea water, where the sea water permittivity has been approximated using a script supplied by Dr. Cathleen Jones at the Jet Propulsion Laboratory. The sea ice permittivity was assumed constant through the sea ice medium to be able to compare the results to the theoretical solution and was taken from the fieldwork data at a depth of 6.2cm.

The frequency that was chosen for the EM-wave in this model is 5.405 GHz, which lies in the *C*-band and is the frequency at which Radarsat-2 operates [Canadian Space Agency, 2011]. The *C*-band was chosen, since it is generally considered to be the optimal choice for sea ice monitoring. [Dierking et al.,

2004] however states that especially for the spring or summer months, when the air temperature is above the freezing point, the penetration depth into the sea ice will be reduced considerably. In the same article it is suggested that for spring/summer months as well as for modeling sea ice ridges and large deformations it might be advantageous to use *L*-band instead of the *C*-band. Since the measurements were taken in the spring the following discussion will also include some modeling with *L*-band frequency.

There are multiple plans to include *L*-band satellites in the next generation of radar remote sensing, such as for example the Tandem-L satellites, which are currently being planned and according to [Krieger et al., 2010] could be launched in 2019. An example of a satellite that was equipped with an *L*-band sensor is the Advanced Land Observing Satellite (ALOS) that, launched by the Japan Aerospace Exploration Agency (JAXA), operated from 2006 to 2011 [Rosenqvist et al., 2014]. ALOS was fitted with a Phased Array L-band Synthetic Aperture Radar (PALSAR) operating at a frequency of 1.270 GHz [Rignot, 2008]. On the 24th of May JAXA launched a successor for ALOS called Advanced Land Observing Satellite-2 (ALOS-2), which is equipped with an enhanced version of the PALSAR called PALSAR-2 [JAXA, 2014]. The frequency that was chosen to represent the L-band scenarios in the following sections has been chosen to be the frequency that ALOS's PALSAR used and which, according to [Rosenqvist et al., 2014], is in the frequency range of PALSAR-2 (1.215 – 1.3 GHz) aboard ALOS-2.

5.1.2 Discussion

To compare the model results with the Fresnel equations, the reflectance can be measured by evaluating the scattering parameter S_{11}. S_{11} is the voltage reflection coefficient at port 1 (the input port) and can be used to find the time average power reflection as $|S_{11}|^2$. The scattering parameter S_{11} is

$$S_{11} = \frac{\sqrt{\text{Power reflected from port 1}}}{\sqrt{\text{Power incident on port 1}}} \tag{5.1}$$

Port 1 can be used, since the top medium (air) does not have an imaginary permittivity part, which means that there will not be any loss in the air medium. If this were not the case the scattering parameter would have to be evaluated using an additional port at the air/sea ice border.

Figure 5.2 shows the time averaged power flux for the *C*-band scenario and for an incidence angle normal to the surface, which is the angle of furthest penetration. Plotting the quantity along a vertical cut-line it can clearly be seen in Figure 5.3 that the power flux dissipates very quickly in the sea ice

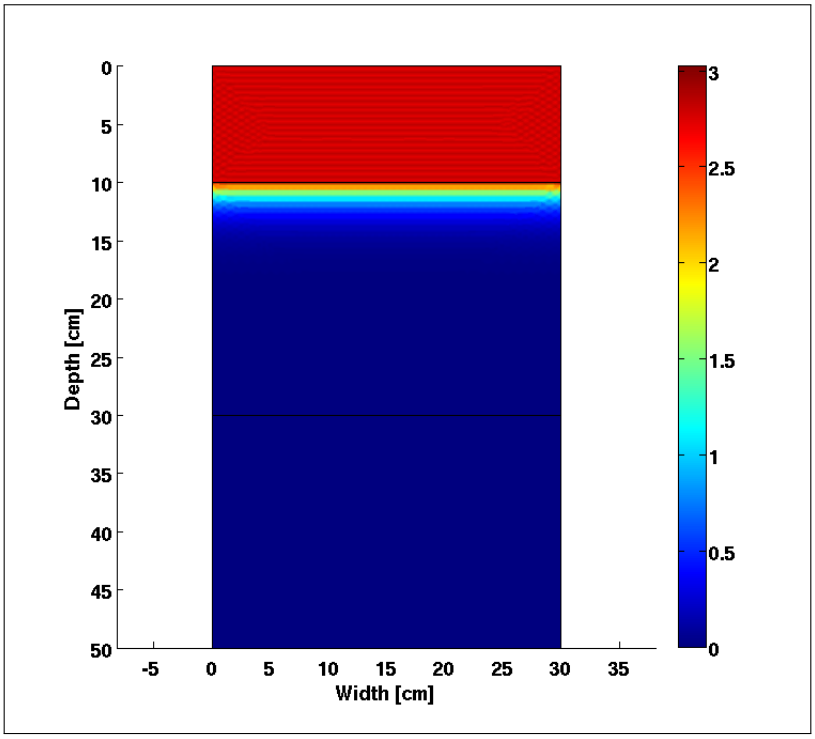

Figure 5.2: Case I: 2D Time averaged power flux for normal incidence angle at C-band frequency.

layer following an exponential curve. It can also be observed that the sea water contribution to the reflection can be neglected for the *C*-band scenario. This is not surprising, since the penetration depth, the depth at which the remaining power is $1/e$ of the incoming power and which can be calculated using equation (2.8), is found to be

$$\delta_p = \frac{\lambda \sqrt{\epsilon'}}{2\pi\epsilon''} \approx 1.9cm \ . \tag{5.2}$$

Inspecting Figure 5.3 it can indeed be seen that the remaining power at 1.9 cm is at $\approx \frac{1}{e}$. The rapid increase and drop in the time averaged power flux at the boundary between the air and the sea ice happens due to superposition of the reflected and incident wave.

For the *L*-band case the penetration length is larger as can be seen from Figure 5.4, which shows the power flux dissipating with depth for the *L*-band scenario. This is due to the fact that equation (2.8) relies on the wavelength, which is larger for the *L*-band than for the *C*-band. It is however important to notice that equation (2.8) also includes the real and imaginary part of the permittivity,

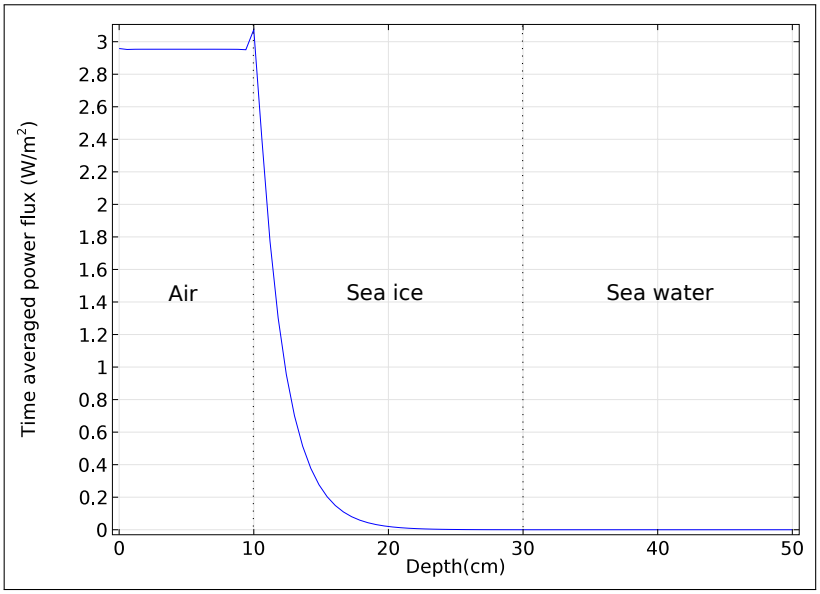

Figure 5.3: Case I: Time averaged power flux for normal incidence angle at C-band frequency along a vertical cut-line in Figure 5.1, indicating the exponential loss of power in the sea ice medium.

which are also both dependent on frequency. The penetration depth for the L-band scenario with the recalculated permittivity values was found to be

$$\delta_p \approx 6.2cm \ . \tag{5.3}$$

This means that the sea water/sea ice boundary will still not have a large effect on the backscatter. This observation can, however, be described as a worst case scenario, since the experimental data has been collected in the spring, when the penetration depth is considerably lower than during the winter. Lower sea ice temperatures generally cause the brine volume size in the ice to decrease causing an increase in brine salinity. As mentioned in section 3.2.3, it is the water molecules and not the ions in the brine that are mainly responsible for the high permittivity at larger temperatures and permittivity will therefore generally be lower at lower temperatures [Shokr, 1998]. Assuming that the density and the salinity of the whole block stays approximately the same, then the penetration depth at $-30°$C for the measurements taken at depth 6.2cm will be 103cm for L-band. This shows that even though the water layer does not play a large role for the spring/summer data gathered during the fieldwork, it can still have a large effect on backscattering during the winter.

Figure 5.5 shows the power dissipation for the C-band scenario on a log scale

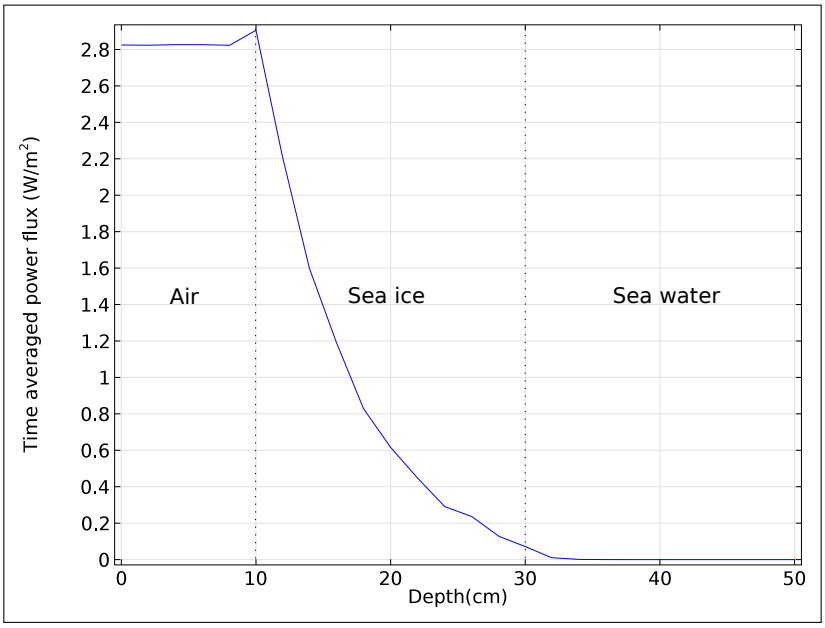

Figure 5.4: Case I: Time averaged power flux for normal incidence angle at L-band frequency along a vertical cut-line in Figure 5.1.

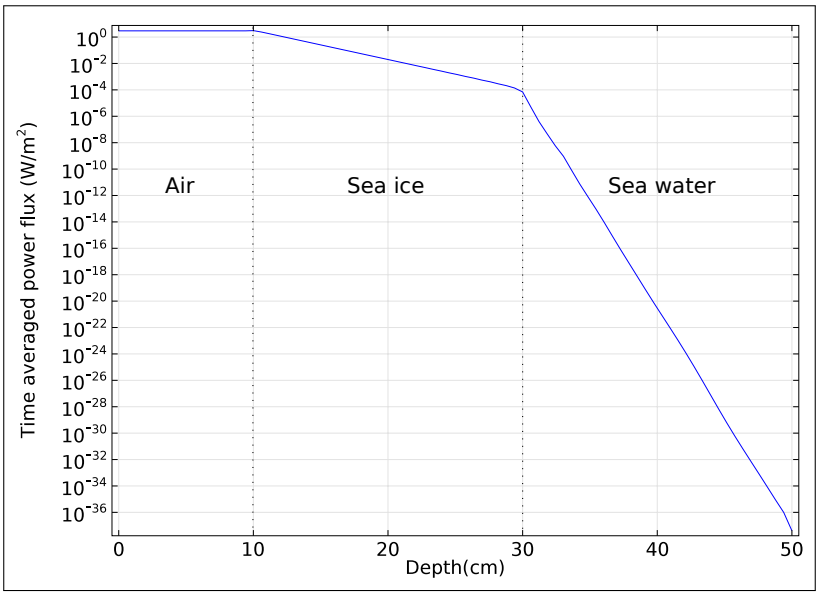

Figure 5.5: Case I: Time averaged power flux at C-band frequencies for normal incidence (Figure 5.3) on a log scale.

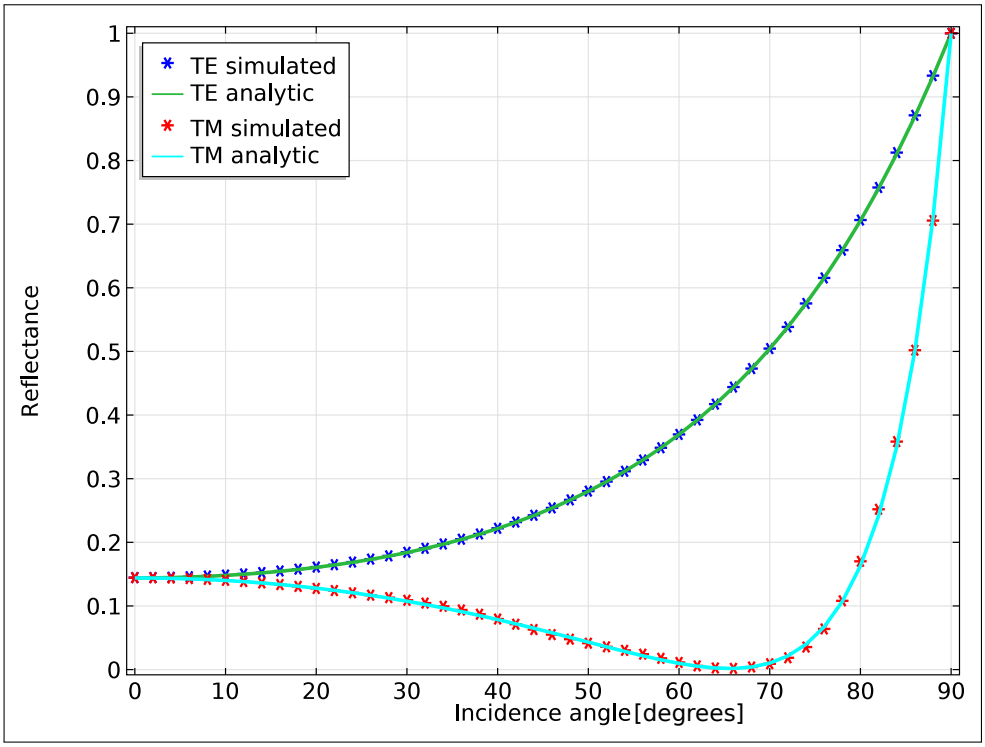

Figure 5.6: Case I: Reflection of the 2-layered medium shown in Figure 5.1. Displaying good agreement between the COMSOL simulations and the analytical solution to the Fresnel equations. The Brewster angle can be observed at $\theta_B \approx 65.5°$

and it can, by the straight lines, clearly be seen that the power dissipates exponentially, which agrees with our expectations. It can also be seen that the power dissipates much more rapidly in the water than in the sea ice, which is due to the large imaginary part of the permittivity of water compared to the sea ice.

Figure 5.6 shows the modeled reflection for both the TE and TM wave, and the analytic solution for the two layer reflection problem. The equations producing the analytic solution can be found in section 4.2.2.

It can be seen from Figure 5.6 that the analytical solution for both TE and TM wave perfectly, within a small numerical tolerance, match the one simulated in COMSOL for the flat infinite surface. This provides confidence in the fact that the model is working correctly. Figure 5.6 also shows a phenomena known as the Brewster angle, the incidence angle (θ) at which the TM-wave is perfectly transmitted, which will be denoted as θ_B. This angle of no reflection can be found as

$$\theta_B = \arctan \frac{n_2}{n_1} \approx 65.5^\circ \,, \tag{5.4}$$

where n_1 and n_2 are the refractive indices for the air and ice material respectively. It can be observed that the analytical solution for the Brewster angle coincides with the simulation results.

5.1.3 Conclusion

The model considered in the previous section agrees well with all the theory that it has been compared to. It was seen from Figure 5.6 that the results for the reflection match perfectly (allowing a small numerical error) with the theoretical solution of the Fresnel equation, which is what should be expected for a flat surface of infinite extent. On the other hand the penetration depth was investigated and it was found that for C-band as well as for L-band the penetration depth for the measured ice properties are quite low due to the high sea ice temperatures. This means, that the bottom part of the ice layers as well as the sea water could theoretically be neglected. Since sea ice at lower temperatures does, however, have much lower permittivity, it is important to keep the water layer to support a variety of sea ice types. Another case where the penetration depth can be considerably larger is for multi-year sea ice, in which large air inclusions replace the brine inclusions.

5.2 Case II: Two layer medium, periodic surface with limited extent

The model considered in this section consists of a two layered medium, where the top layer represents sea ice and the bottom layer sea water. The sea ice layer is fitted with a periodic surface to validate the model with help of the Bragg scattering phenomena.

5.2.1 Description

The model geometry in the previous section has been updated for this model to be able to extract the angular distribution of the scattered waves and is presented in Figure 5.7. Due to these geometric changes the model can not utilize ports, as described in section 5.1, but instead requires the definition of a global plane wave, as described in section 4.1. A PML (see section 4.1.5) surrounded by a perfectly conducting boundary condition is used to restrict the domain of

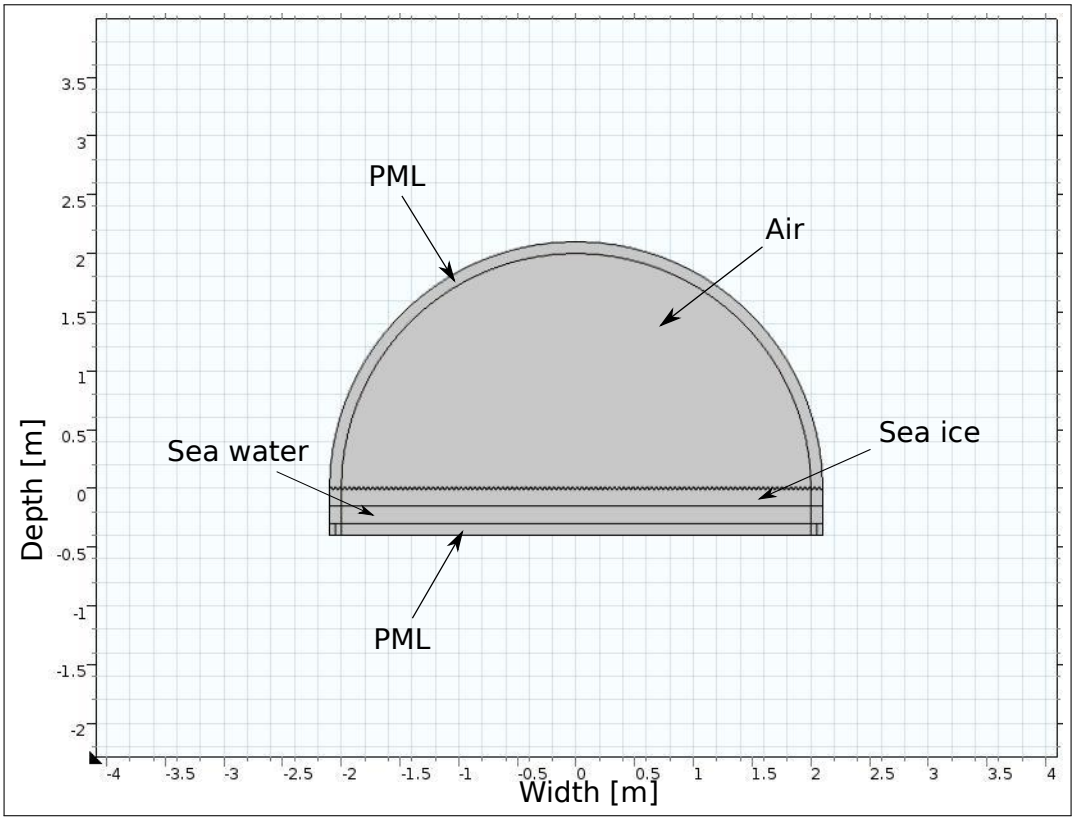

Figure 5.7: Case II: Two layer model geometry with a periodic top surface.

interest and the Far-field has been calculated to find the backscattering cross section as described in section 4.1.7. Instead of solving for the full field this model, as well as all the models discussed in the later sections, utilizes the scattered field formulation. This makes it possible to define the global plane wave to be directly incident onto the scatterer, thus making it easier to define the plane wave excitation. The rough surface in this model is specifically set up to cause a phenomena called Bragg scattering, which is used to qualitatively validate the modified model.

Bragg scattering or Bragg resonance is a phenomena that, under certain conditions, can be observed for periodic surfaces. It occurs, when the radar wavelength and the surface wavelength conform to the Bragg resonance condition, which is

$$\lambda_s = \frac{n\lambda_r}{2sin(\theta)} \ , \tag{5.5}$$

where λ_s is the surface wavelength, λ_r the radar wavelength, θ the incidence

angle and n an integer.

According to the theory presented in [Phillips, 1989] the backscatter will be considerably larger if the Bragg resonance condition is met compared to the other angles. One application, where Bragg scattering is a common phenomena, is the observation of the ocean surface, which generally appears dark in a SAR image. In case of small wind-stresses the ocean surface can instead appear brighter if the condition in (5.5) is met. Considering equation (5.5) it can be seen that for radar images (usually with wavelength on an order of cm) the backscattering cross section is highly sensitive to roughness caused by small wavelengths.

To cause this form of scattering, the surface was chosen to be a sinusoid of shape

$$y = 0.01sin\left(\frac{2\pi x}{\lambda_s}\right)[meter]\,, \tag{5.6}$$

where y is the height of the surface, x are the coordinates along the x-axis and λ_s is the wavelength of the surface defined as $\frac{\lambda_r}{2sin(45°)}$ with λ_r being the wavelength of the satellite, which in this case was chosen to match the wavelength of Radarsat-2. According to equation (5.5) and the surface parameters chosen, the surface should cause first order Bragg scattering at $\theta_{45°}$.

5.2.2 Discussion

The backscattering cross section, for the surface that has been generated according to the description in the previous section, can be seen in Figure 5.8. The backscattering cross section has not been normalized to the backscatter coefficient as a meaningful way to normalize the 1-D surface (in the 2-D model) was not found.

The Bragg resonance around 45° can clearly be seen in Figure 5.8, which coincides with our expectations. It is also possible to see a peak at 0°, which is related to the sinusoidal symmetry of the surface. The small spikes between the two main peaks are believed to be caused mainly by the discretization error that FEM introduces by representing the sinusoid boundary using triangular elements. This error is however not necessarily unrealistic, since real scenarios tend to not contain perfectly smooth sinusoids either.

Looking at the 45° case in particular, Figure 5.9 shows the angular distribution of the Far field. Beside the large peak caused by Bragg resonance at the Bragg angle (45°), a large peak can be seen in the direction of specular reflection (135°). Looking more closely, zooming in, at the angular distribution (Figure

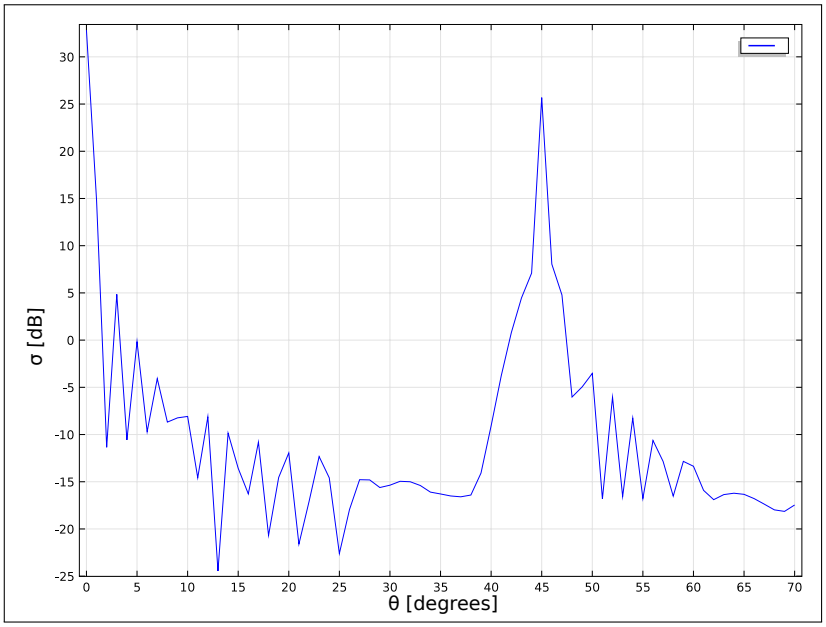

Figure 5.8: Case II: Backscattering cross section of the 2-layered medium plotted vs. the incidence angle, clearly showing the expected Bragg resonance at 45° (and 0°).

5.10) it is possible to see that there is evidence for small side lobes, which are believed to be caused by the FEM approximation. A denser meshing could presumably decrease the effects of these side lobes, but, since the side lobes magnitude is neglectable compared to the Bragg resonance and the specular component, it is not practical to improve this at the cost of performance.

5.2.3 Conclusion

The rough periodic surface that was considered in this section has been used to qualitatively validate the model that has been created as part of this thesis by modeling Bragg scattering. According to the theory the results showed that the magnitude of the backscattering cross section increased considerably when equation (5.5) was satisfied.

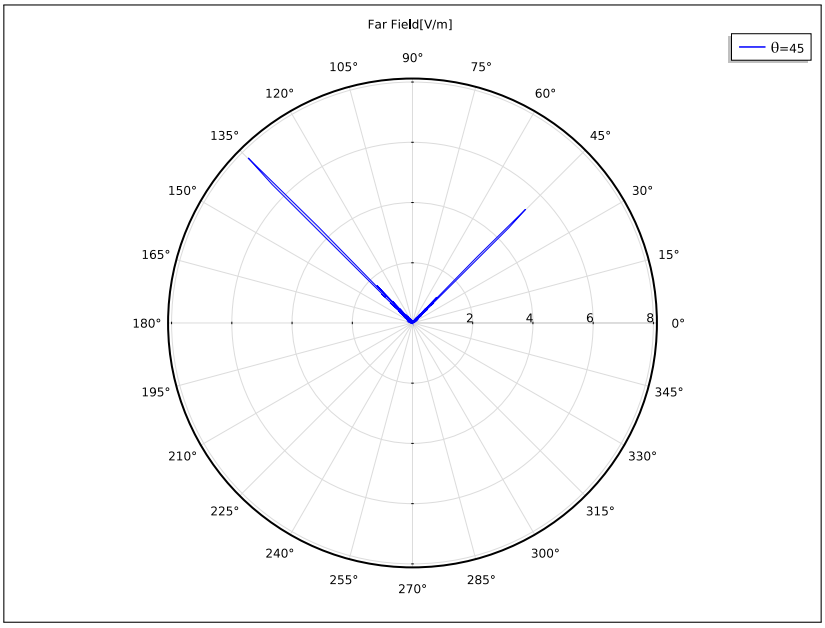

Figure 5.9: Case II: Angular distribution of the Far field for a 45° incidence angle.

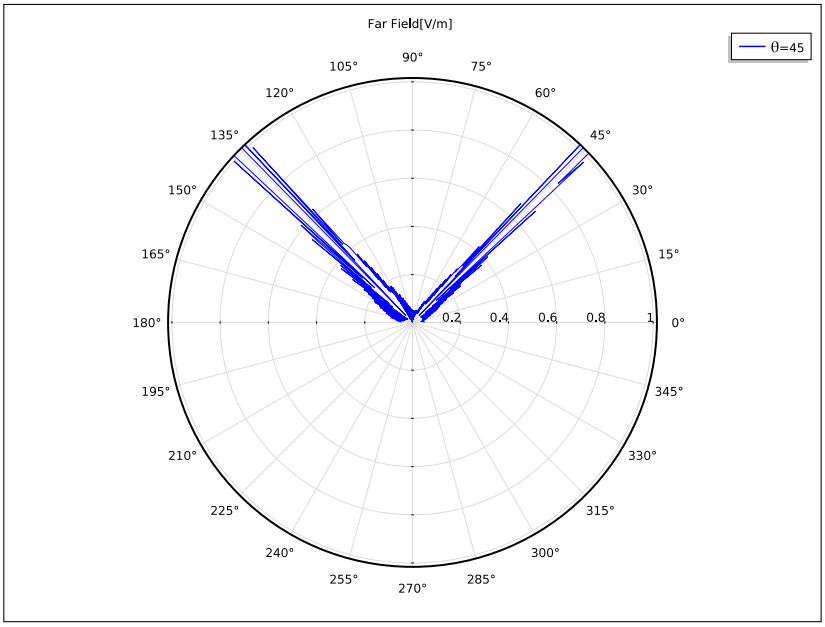

Figure 5.10: Case II: Angular distribution of the Far field for a 45° incidence angle: Zoomed scale from Figure 5.9.

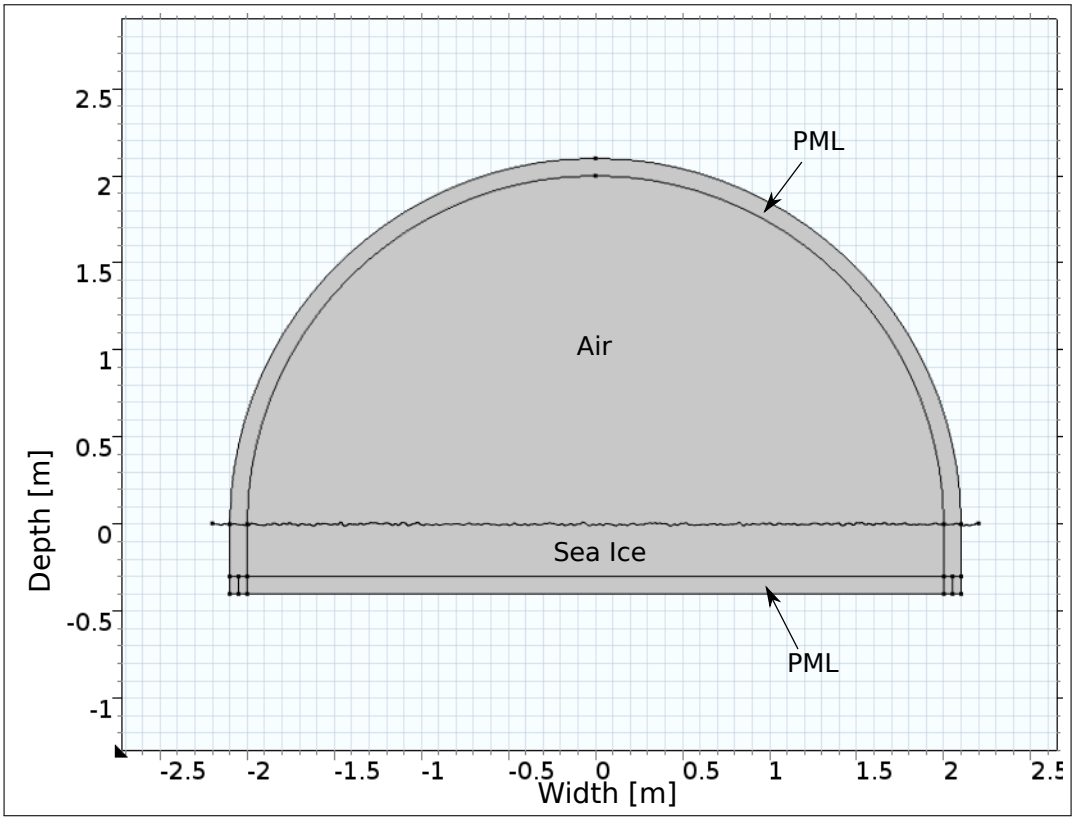

Figure 5.11: Case III: Geometry for the one layered, slightly rough surface.

5.3 Case III: One layer medium, small surface roughness with limited extent

The model considered in this section consists of a one layered medium with a small surface roughness and aims to compare the model results to a common scattering model, the SPM.

5.3.1 Description

The setup of the model in this section is similar to the one described in section 5.2. The main difference is that the periodic surface has been replaced with a random generated surface with a correlation length of $1.5cm$ and a RMS height of $0.04cm$. The correlation function chosen was Gaussian as described in section 4.2.3. Apart from that, the only other difference is that only one layer is considered in this case to be able to compare it to a simple existing scattering model. The final geometry of this model is displayed in Figure 5.11.

Due to the lack of an analytical solution an attempt was made to evaluated the result by comparing it to the SPM for the same surface correlation length and RMS height. The SPM is a scattering model that is only valid when the surface roughness is small, which, as discussed in section 3.1.4, means small relative to the radar wavelength. The domain in which the SPM is valid, is, according to [Fung and Chen, 2010], defined as

$$ks_h < 0.3 \,, \tag{5.7}$$

$$kl < 3 \,, \tag{5.8}$$

and

$$\frac{s_h}{l} < 0.3 \,, \tag{5.9}$$

where k is the wavenumber, s_h is the RMS height of the surface and l is the correlation length.

For further information on the SPM the reader is referred to Appendix B and [Fung and Chen, 2010].

The case can be split up into two separate parts, where the first one focuses on analyzing changes in the backscatter cross section for frequency changes at constant permittivity. The second part does the same, but keeps the frequency constant and varies permittivity.

5.3.2 Discussion

Figure 5.12 shows the results for the SPM model, when run for two different frequencies and Figure 5.13 shows the modeled results for the same frequencies. As stated in section 5.2.2 the backscattering cross section results of the model are not normalized and it is therefore not expected that they numerically match the backscatter results of the SPM.

Inspecting and comparing the two figures does, at first glance, not show any similarities. This is as expected, however, since the implemented model only represents one realization of the statistical parameters, the correlation length and the RMS height, whereas the SPM model estimates the backscatter coefficient average of all possible realizations. For a large number of realizations the shape of the average model solution is expected to be very similar to the SPM solution, this could, however, not be tried due to the large amount of realizations required and the large runtime of the model. It can, however, be seen that the lower frequency ($5.1GHz$) case tends to have lower backscattering

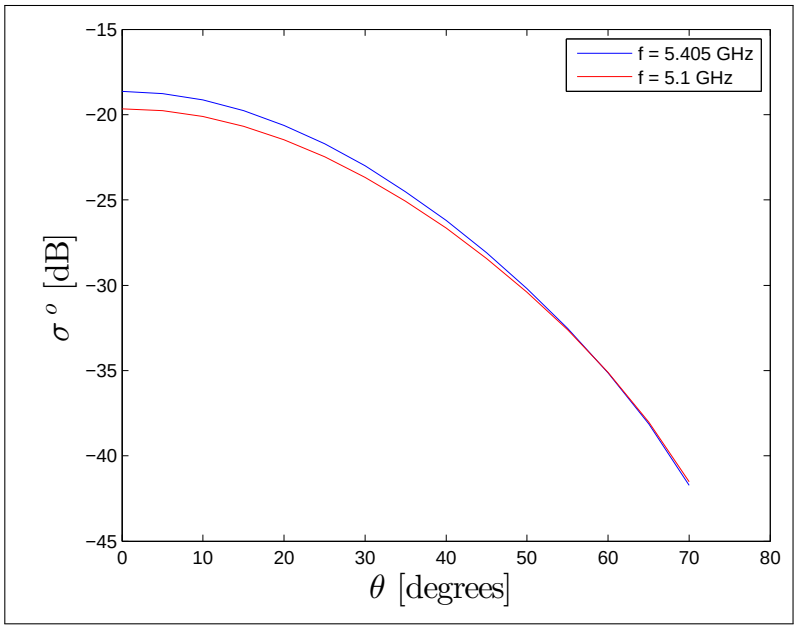

Figure 5.12: Case III: Backscatter coefficient for the slightly rough surface vs. incidence angle for two frequency values using the SPM.

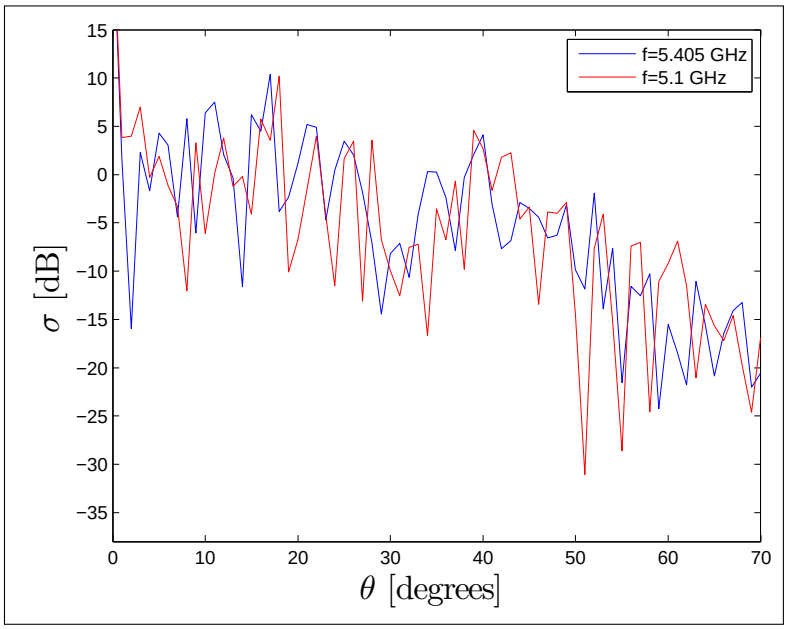

Figure 5.13: Case III: Backscattering cross section for the slightly rough surface vs. incidence angle for the two frequency values using the model developed as part of this thesis.

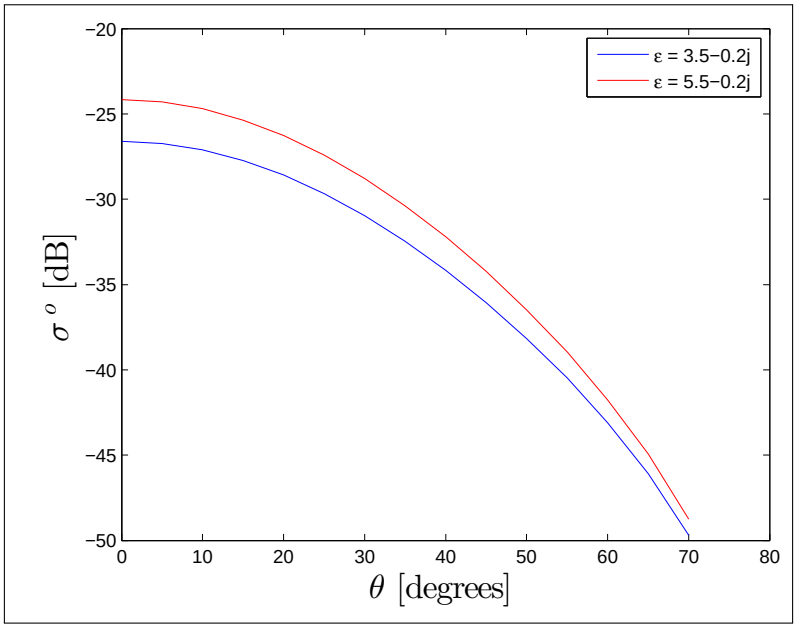

Figure 5.14: Case III: Backscatter coefficient for the slightly rough surface vs. incidence angle for two permittivity values using the SPM.

cross section results in the model, which coincides well with the results of the SPM model. For larger incidence angles a considerable decrease in backscatter, both in the model results as well as the SPM results, can be noticed.

Figure 5.14 shows the results for the SPM model and Figure 5.15 shows the modeled backscattering cross section results for the second part of the case. In this part, however, as previously stated, the frequency is kept constant at the frequency of Radarsat-2 and the permittivity is varied instead. It can again be seen that the results are not as smooth as the SPM curve, but it is still possible to see that the backscatter for the higher permittivity is generally higher than the backscatter of the lower permittivity both in the model and in the SPM. It is also in this case possible to see the downward trend in the backscatter or backscattering cross section level as the incidence angle increases.

5.3.3 Conclusion

In this case the results of the model have been compared to the SPM, a scattering model that is one of the most widely used backscatter models in remote sensing. Due to the lack of normalization and due to the fact that the model that was implemented as part of this thesis only models one realization of the statistical surface parameters, it was difficult to numerically compare the re-

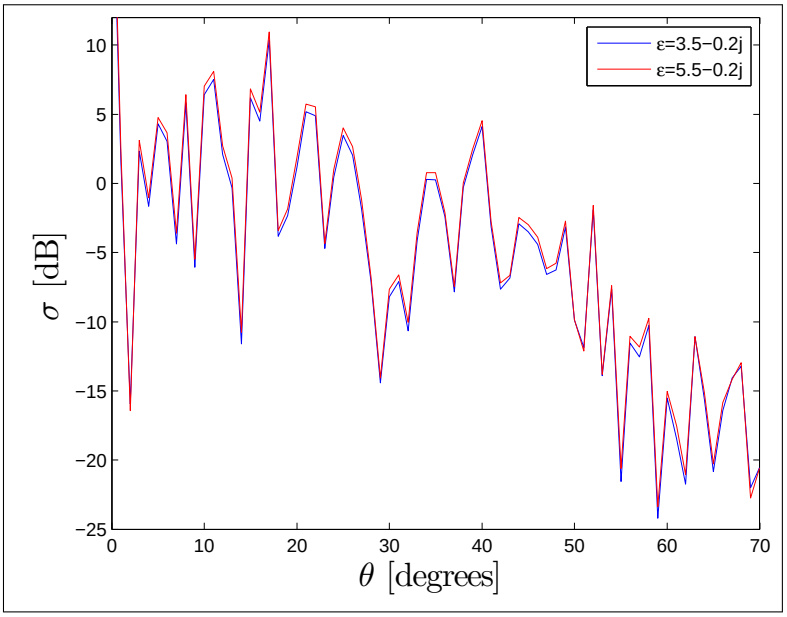

Figure 5.15: Case III: Backscattering cross section for the slightly rough surface vs. incidence angle for the two permittivity values using the model developed as part of this thesis.

sults for the two models. It was possible, however, to validate the model by comparing the characteristics of both the SPM and the implemented model. Doing this, it could be seen that the model qualitatively agrees well with the analytical model.

5.4 Case IV: One layer medium, very rough surface with limited extent

In this section the backscattering cross section of a very rough surface is being modeled and compared to the results from section 5.3 (Case III).

5.4.1 Description

This section extends the previous case by exchanging the previous surface with a surface of larger roughness. The statistical parameters of this surface were chosen to be a correlation length of 1.5 cm and a RMS height of 4 cm. Compared to the surface discussed in section 5.3, a surface with these parameters can be considered to be on the opposite end of the roughness spectrum. For

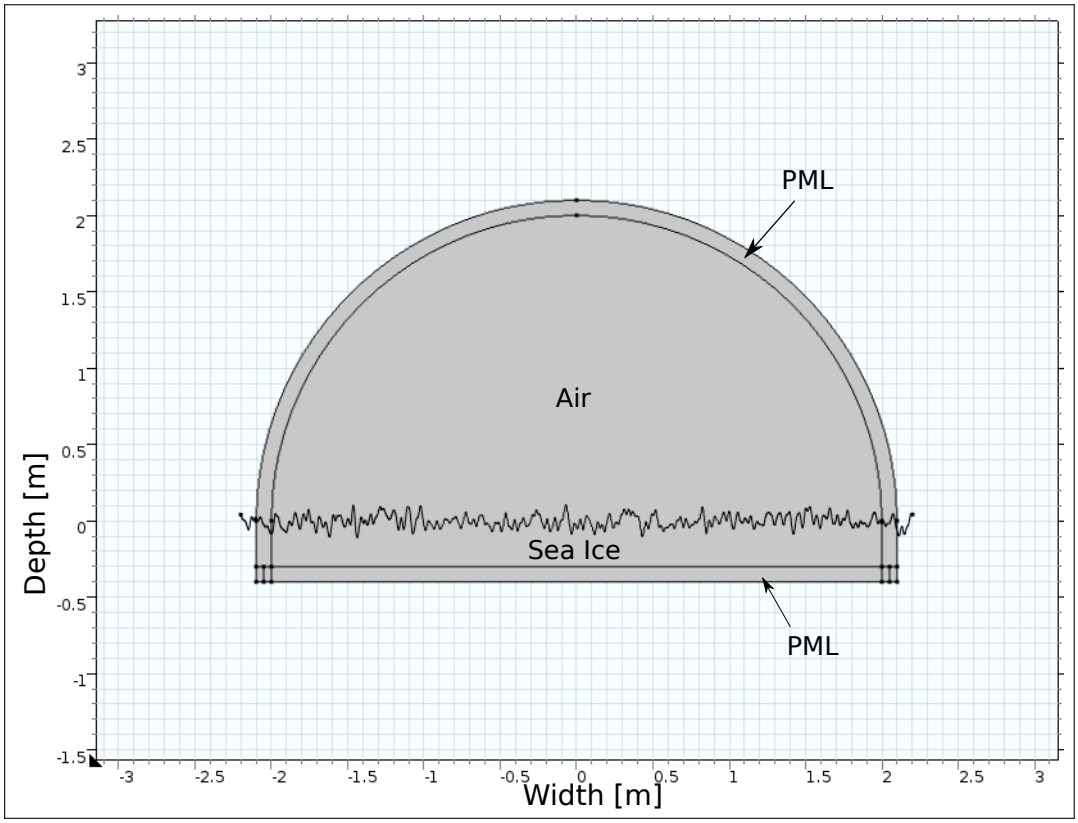

Figure 5.16: Case IV: Geometry for the one layered extremely rough surface

these surfaces the SPM is not valid, as the statistical parameters lie outside of the validity domain given by the equations (5.7), (5.8) and (5.9). The model geometry with the new surface is shown in Figure 5.16.

5.4.2 Discussion

The model was run for the same scenarios as in the previous section. Figure 5.17 shows the result for the frequency of Radarsat-2 and a frequency of 5.1 GHz. The medium modeled has a complex permittivity of $3.5 - 0.2i$. The results displayed in Figure 5.18 are for two media with different permittivities at constant (Radarsat-2) frequency. It can be seen from the figures that the drop in the backscattering cross section, which was seen in section 5.3, is considerably smaller than in the Figures 5.17 and 5.18. This agrees with our expectations as extreme roughness will cause large variations in the local incidence angle and will therefore lead to a more uniform scattering pattern. As the roughness is further increased, the scattering pattern will become completely independent of the incidence angle and, as stated in section 3.2.1, the surface will approach

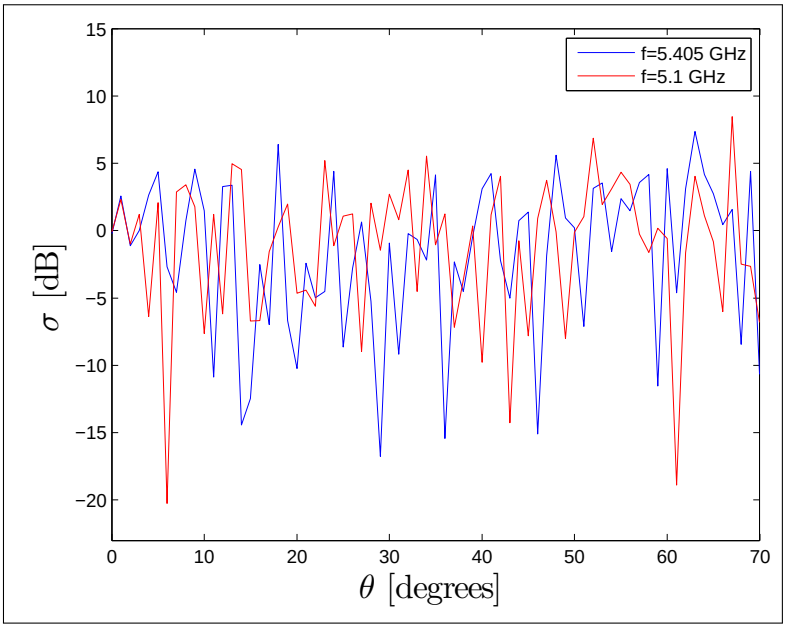

Figure 5.17: Case IV: Backscattering cross section for the very rough surface vs. incidence angle for the two frequency values using the model developed as part of this thesis.

a Lambertian surface. It can also be seen that a larger permittivity, as seen in the previous case, still results in a larger backscattering cross section.

5.4.3 Conclusion

In this case the model was changed to represent an extremely rough surface and it was seen that the drop in the backscattering cross section with an increase in incidence angles is considerably smaller for the rough surface than it was for the small roughness scenario discussed in the previous section. This agrees well with the notion that perfectly rough Lambertian surfaces have uniform scattering patterns.

5.5 Case V: Two layer medium, rough surface with limited extent

In this section the backscatter of a sea ice layer with a rough surface on top of sea water is measured.

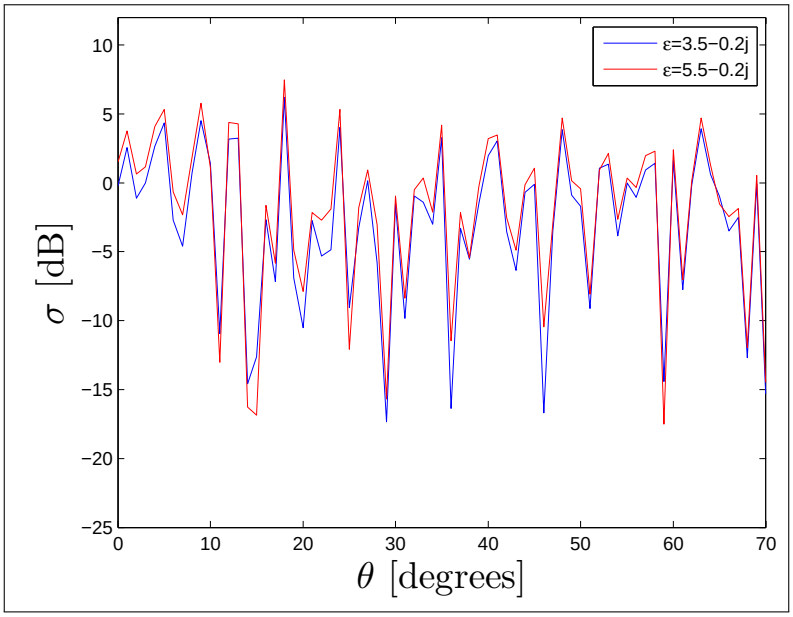

Figure 5.18: Case IV: Backscattering cross section for the very rough surface vs. incidence angle for the two permittivity values using the model developed as part of this thesis.

5.5.1 Description

This section modifies the previously discussed models to include both a sea ice and sea water layer at C-band frequency (Radarsat-2). Figure 5.19a displays the geometry for this scenario, where the surrounding layer is a PML. The scenario utilizes the fieldwork results presented in section 4.2.1 and lets the permittivity of the sea ice vary continuously with depth as shown in the Figures 4.6a and 4.6b. The profiles for the salinity (S), temperature (T), density (D) and for the real (ϵ') and imaginary part (ϵ'') of the permittivity have, for completeness, been included in this section as small thumbnails in Figure 5.19.

As no surface profile of the sea ice section is available the author has decided to make use of the statistical surface parameters that were found in [Drinkwater, 1989] for smooth ice. These are displayed in Table 2.1.

A scenario of this type has, to the authors knowledge, not been modeled previously.

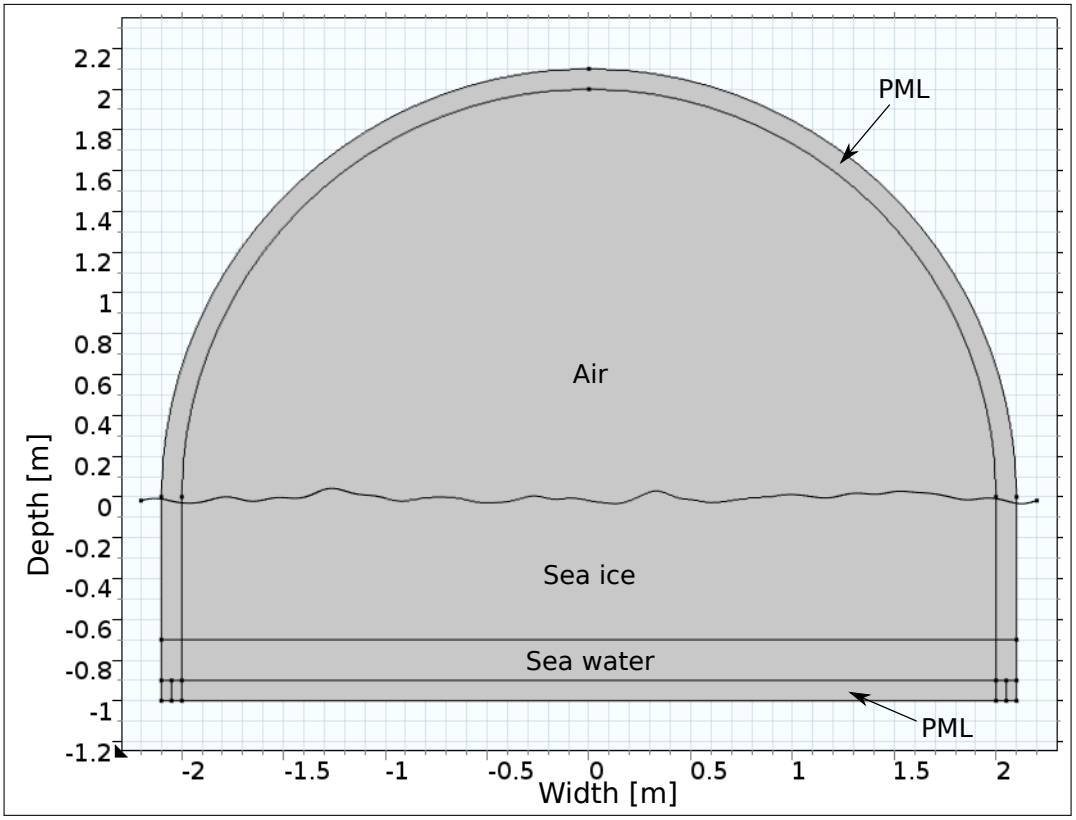

(a) Case V: Geometry for the 2 layered scenario.

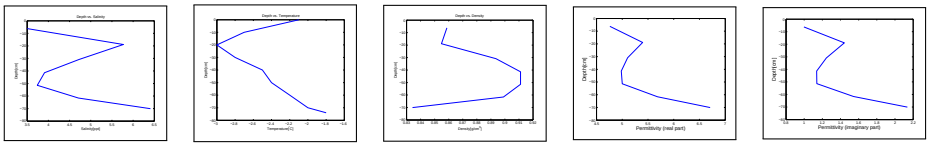

(b) S **(c)** T **(d)** D **(e)** ϵ' **(f)** ϵ''

Figure 5.19: Case V: Geometry for the two layered surface with varying permittivity. The TDS profiles and the permittivity profile that were used and that correspond to the core taken in Van Keulenfjord (described in section 4.2.1) have been included in Figures (b) to (f).

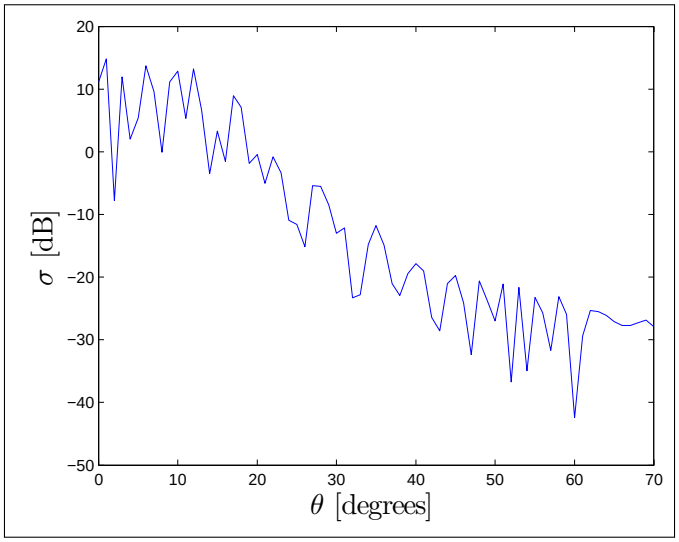

Figure 5.20: Case V: Backscattering cross section results for the two layered scenario plotted versus the incidence angle.

5.5.2 Discussion

Figure 5.20 shows the backscattering cross section for the modeling scenario. As expected the backscattering cross section, for this reasonably smooth surface, varies considerably for the range of incidence angles. As discussed in case I in section 5.1 the penetration depth for C-band is extremely small for the measured conditions and it is not expected that the sea water/sea ice boundary has a large effect on the backscattering cross section.

5.5.3 Conclusion

The model considered in this case combines all previously discussed ideas into one single model. As this is a more complicate case, it was not possible to compare it to existing models. However, based on the previous validations we assume that the model performs correctly and that the backscattering cross section result, when normalized, does in fact coincide with what a pixel of an image at that location at that point in time would have looked like for the given surface.

6

Conclusion

6.1 Summary

In this thesis, a numerical model has been designed that uses the FEM to model the backscattering cross section from rough multi-layered sea ice surfaces and incorporates TDS fieldwork measurements to estimate the continuous sea ice permittivity profile using the Polder-van-Santen/de Loor mixture model. Figure 6.1 provides an overall view over the model and shows how the fieldwork data, radar frequencies and surface parameters (RMS and correlation length) are used as input data to the permittivity and surface models. The output from these models is imported into COMSOL and used to define the geometry of the model as well as the material properties. Once the physics have been defined and the meshing has been performed the modeling can begin and will produce the modeling results such as, for example, the backscattering cross section profiles that were shown in the previous chapter.

The model was designed as general as possible, allowing it to be adapted to different surfaces and different materials as well as frequencies. The model has been successfully validated using established theory such as the Fresnel equations, which showed a perfect agreement with the modeled results, as well as using common phenomenas such as Bragg resonance. It was also compared to the SPM and, apart from the backscatter normalization, clear similarities were observed. An extremely rough surface was then modeled and qualitatively compared to the SPM case. It showed the characteristics that can be expected from a rough surface.

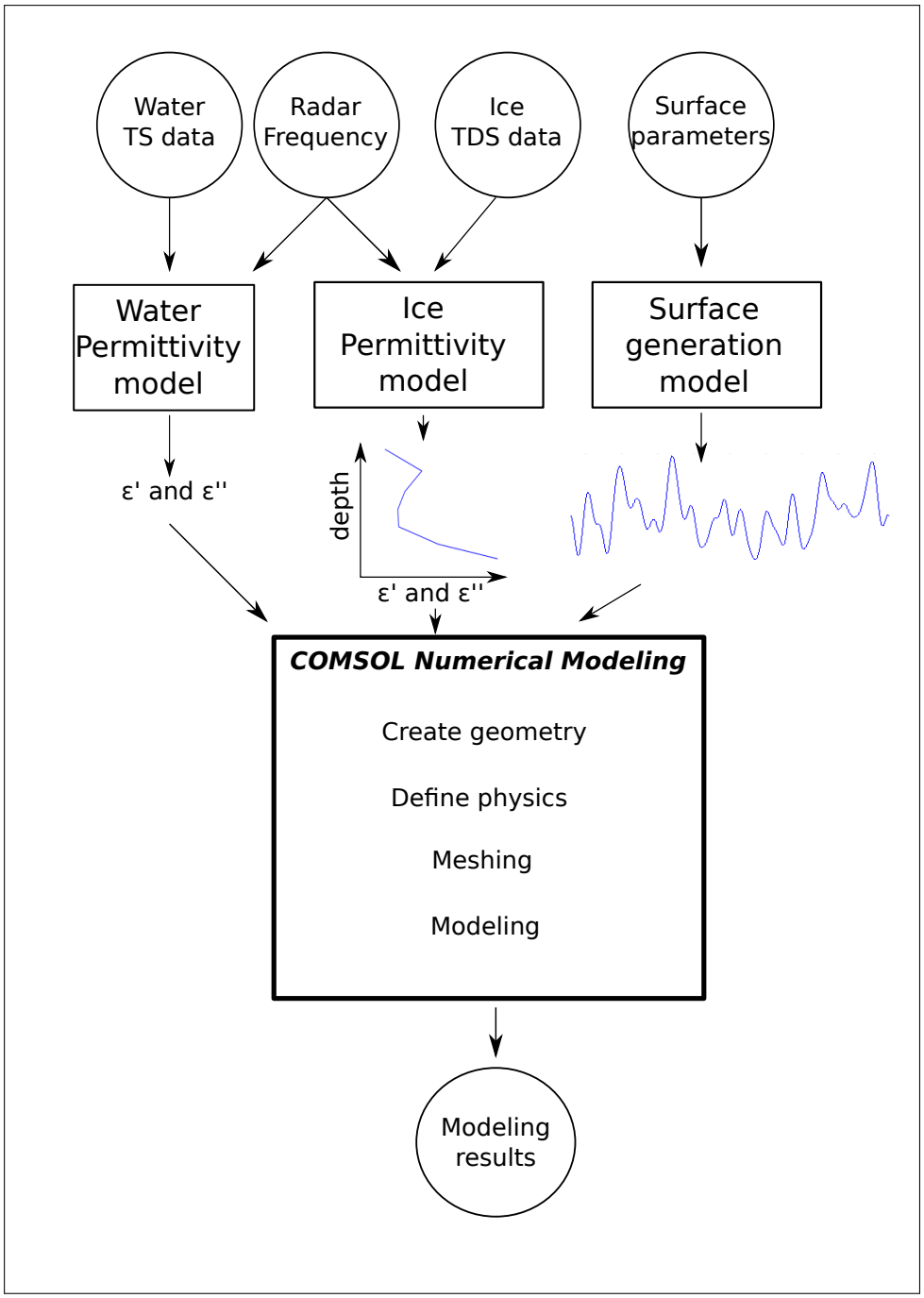

Figure 6.1: Design model that provides an overview of how the different model components (represented by squares) interact with each other and what data (represented by circles) they require as input. TS in the above figure is used to denote the temperature and salinity of the sea water.

Basing the trust in the model on the successful validations, the backscatter of a two layered sea ice/sea water scenario was modeled. In this scenario the frequency at which Radarsat-2 operates was chosen, as *C*-band is generally considered the optimal choice for sea ice monitoring. TDS measurements taken from first year sea ice in the Svalbard region were included to model the sea ice with a continuous permittivity profile. The surface was generated as a random Gaussian surface with correlation lengths and RMS heights that were found in the literature for first year sea ice since no surface roughness measurements were taken during the fieldwork. To the authors knowledge such a scenario has not been modeled previously.

6.2 Future work

There are many improvements and extensions to the model that could not be added due to time constraints. Some of these will be discussed in this section.

Although the model executes well its computational performance of ≈ 4 hours per pixel is too high to be practical and time should be spent on improving said performance by evaluating the possibility of using symmetrical geometry or by reducing the meshing domain. Increased computational performance could be utilized to run the model a large number of times for different surface realizations with the same statistical surface parameters and comparing the mean of all of the backscattering cross section results to the SPM. It is expected that for a large number of realizations the shape of the backscattering cross section will approach the SPM solution. Repeated realizations could, on the other hand, also be used to study speckle statistics. In addition, increased performance might offer the possibility to model a 3D domain instead of just the 2D domain, which would allow for meaningful normalizing of the backscattering cross section.

The model should also be extended to support large air and brine inclusions. Especially air inclusions for multi-year sea ice are commonly too large to still allow the sea ice to be modeled as a homogeneous medium at *C*-band frequencies and must therefore be modeled by explicitly including them into the geometry. Combining the implemented model with a model for sea ice growth might have to be considered to achieve this.

As most of the time available for this thesis was spend on designing and validating the model, future work includes the actual use of the model for scenarios that might not yet be completely understood. This can involve tuning of parameters, such as the frequency, and analyzing the effects, but it can also involve

comparing effects of different polarizations. The current model only supports horizontal polarization, but future work will be conducted on supporting vertical polarization as well.

The benefit of designing the model as general as possible is that additional layers can be added to it easily. This can be useful in the future to model, for example, the effect of oil under the sea ice, which is a research area of growing interest. As the amount of ground truth data in this field is very limited, numerical models will have to be used to test theories and assumptions.

On a different note the model could be extended to more generally represent the SAR geometry by introducing chirps and by combining the separate pixels to an images. This is however tightly coupled to improvements in computational performance, since it is currently not feasible to model more than a few pixels.

6.3 Conclusion

From this work it can be concluded that the modeling performs well and produces results that match the theory. It provides a great starting point to numerical modeling of sea ice and other media under realistic conditions. A lot more work is, however, required both in validating as well as in extending the model.

Bibliography

[Beckmann and Spizzichino, 1963] Beckmann, P. and Spizzichino, A. (1963). *The scattering of electromagnetic waves from rough surface*. Pergamon.

[Berenger, 1994] Berenger, J.-P. (1994). A perfectly matched layer for the absorption of electromagnetic waves. *Journal of computational physics*, 114(2):185–200.

[Bern and Plassmann, 1997] Bern, M. W. and Plassmann, P. E. (1997). *Mesh generation*. Pennsylvania State University, Department of Computer Science and Engineering, College of Engineering.

[Bohren and Huffman, 1998] Bohren, C. F. and Huffman, D. R. (1998). *Absorption and scattering of light by small particles*. John Wiley & Sons.

[Canadian Space Agency, 2011] Canadian Space Agency (2011). Radarsat-2 satellite characteristics. http://www.asc-csa.gc.ca/eng/satellites/radarsat/radarsat-tableau.asp. Accessed: 2014-04-18.

[Carlström, 1995] Carlström, A. (1995). *Modelling microwave backscattering from sea ice for Synthetic-Aperture Radar applications*. PhD thesis, Chalmers University of Technology.

[Chew and Weedon, 1994] Chew, W. C. and Weedon, W. H. (1994). A 3d perfectly matched medium from modified maxwell's equations with stretched coordinates. *Microwave and optical technology letters*, 7(13):599–604.

[Chuvieco et al., 2009] Chuvieco, E., Huete, A., et al. (2009). *Fundamentals of satellite remote sensing*. CRC Press Inc.

[Collin, 2001] Collin, R. E. (2001). *An IEEE Press Classic Reissue:"Foundations For Microwave Engineering"*. IEEE Press Series on Electromagnetic Wave Theory, IEEE, Wiley-Interscience.

[Comiso, 2006] Comiso, J. C. (2006). Arctic warming signals from satellite

observations. *Weather*, 61(3):70–76.

[COMSOL, 2012] COMSOL (2012). *RF Module User's Guide*. COMSOL.

[Courant et al., 1943] Courant, R. et al. (1943). Variational methods for the solution of problems of equilibrium and vibrations. *Bull. Amer. Math. Soc*, 49(1):1–23.

[Cox and Weeks, 1983] Cox, G. and Weeks, W. (1983). Equations for determining the gas and brine volumes in sea-ice samples. *Journal of Glaciology*, 29:306–316.

[De Loor, 1968] De Loor, G. (1968). Dielectric properties of heterogeneous mixtures containing water. *J. Microwave Power*, 3(2):67–73.

[Dierking et al., 2004] Dierking, W., Skriver, H., and Gudmandsen, P. (2004). What is gained by using an l-band sar for sea ice monitoring? In *Proc. ENVISAT/ERS Symposium*, pages 6–10.

[Drinkwater, 1989] Drinkwater, M. R. (1989). Limex'87 ice surface characteristics: Implications for c-band sar backscatter signatures. *Geoscience and Remote Sensing, IEEE Transactions on*, 27(5):501–513.

[Dubois et al., 1995] Dubois, P. C., Van Zyl, J., and Engman, T. (1995). Measuring soil moisture with imaging radars. *Geoscience and Remote Sensing, IEEE Transactions on*, 33(4):915–926.

[Elachi and Van Zyl, 2006] Elachi, C. and Van Zyl, J. J. (2006). *Introduction to the physics and techniques of remote sensing*, volume 28. Wiley.

[Eppler et al., 1992] Eppler, D. T., Farmer, L. D., Lohanick, A. W., Anderson, M. R., Cavalieri, D. J., Comiso, J., Gloersen, P., Garrity, C., Grenfell, T. C., Hallikainen, M., et al. (1992). Passive microwave signatures of sea ice. *Geophysical Monograph Series*, 68:47–71.

[ESA, 2014] ESA (2014). Mission Details - Sentinel-1. https://earth.esa.int/web/guest/missions/esa-future-missions/sentinel-1. Accessed: 2014-05-14.

[Feinberg, 1944] Feinberg, E. (1944). On the propagation of radio waves along an imperfect surface. *J. Phys.(Moscow)*, 8:317–330.

[Freeman and Durden, 1998] Freeman, A. and Durden, S. L. (1998). A three-component scattering model for polarimetric sar data. *Geoscience and Remote*

Sensing, IEEE Transactions on, 36(3):963–973.

[Fung and Chen, 2010] Fung, A. and Chen, K. (2010). *Microwave Scattering and Emission Models for Users*. The Artech House remote sensing series. Artech House, Incorporated.

[Fung et al., 2002] Fung, A., Liu, W., Chen, K., and Tsay, M. (2002). An improved iem model for bistatic scattering from rough surfaces. *Journal of Electromagnetic Waves and Applications*, 16(5):689–702.

[Fung et al., 1992] Fung, A. K., Li, Z., and Chen, K. (1992). Backscattering from a randomly rough dielectric surface. *Geoscience and Remote Sensing, IEEE Transactions on*, 30(2):356–369.

[Haas, 2010] Haas, C. (2010). Dynamics versus thermodynamics: The sea ice thickness distribution. *Sea Ice*, 2:113–151.

[Hallikainen, 1977] Hallikainen, M. (1977). Dielectric properties of sea ice at microwave frequencies. *NASA STI/Recon Technical Report N*, 78:11293.

[Hallikainen and Winebrenner, 1992] Hallikainen, M. and Winebrenner, D. P. (1992). The physical basis for sea ice remote sensing. *Geophysical Monograph Series*, 68:29–46.

[Harrington, 1967] Harrington, R. F. (1967). Matrix methods for field problems. *Proceedings of the IEEE*, 55(2):136–149.

[Henderson et al., 1998] Henderson, F. M., Lewis, A. J., et al. (1998). *Principles and applications of imaging radar. Manual of remote sensing, volume 2*. John Wiley and sons.

[Ho, 2010] Ho, J. (2010). The implications of arctic sea ice decline on shipping. *Marine Policy*, 34(3):713–715.

[Hoekstra and Cappillino, 1971] Hoekstra, P. and Cappillino, P. (1971). Dielectric properties of sea and sodium chloride ice at uhf and microwave frequencies. *Journal of Geophysical Research*, 76(20):4922–4931.

[Hossain et al., 2012] Hossain, M. et al. (2012). Polarimetric synthetic aperture radar measurements of snow covered first-year sea ice.

[Imperatore et al., 2009] Imperatore, P., Iodice, A., and Riccio, D. (2009). Electromagnetic wave scattering from layered structures with an arbitrary number of rough interfaces. *Geoscience and Remote Sensing, IEEE Transactions*

on, 47(4):1056–1072.

[JAXA, 2014] JAXA (2014). Launch Result of H-IIA Launch Vehicle No. 24 with "DAICHI-2" (ALOS-2) onboard - Press Release. http://global.jaxa.jp/press/2014/05/20140524_h2af24.html. Accessed: 2014-05-24.

[Jensen, 2009] Jensen, J. R. (2009). *Remote Sensing of the Environment: An Earth Resource Perspective 2/e*. Pearson Education India.

[Jin et al., 2002] Jin, J.-M., Jin, J., and Jin, J.-M. (2002). *The finite element method in electromagnetics*. Wiley New York.

[Johannessen et al., 2006] Johannessen, O. M., Alexandrov, V., Frolov, I. Y., Sandven, S., Pettersson, L. H., Bobylev, L. P., Kloster, K., Smirnov, V. G., Mironov, Y. U., and Babich, N. G. (2006). *Remote sensing of sea ice in the Northern Sea Route: studies and applications*. Springer.

[Johansson and Askne, 1987] Johansson, R. and Askne, J. (1987). Modelling of radar backscattering from low-salinity ice with ice ridges. *International Journal of Remote Sensing*, 8(11):1667–1677.

[Kim et al., 1985] Kim, Y., Moore, R., Onstott, R., and Gogineni, S. (1985). Towards identification of optimum radar parameters for sea ice monitoring. *Journal of Glaciology*, 31(109):214–219.

[Komarov et al., 2014] Komarov, A. S., Shafai, L., and Barber, D. G. (2014). Electromagnetic wave scattering from rough boundaries interfacing inhomogeneous media and application to snow-covered sea ice. *Progress In Electromagnetics Research*, 144:201–219.

[Krieger et al., 2010] Krieger, G., Hajnsek, I., Papathanassiou, K., Eineder, M., Younis, M., Zan, F. D., Lopez-Dekker, P., Huber, S., Werner, M., Prats, P., et al. (2010). Tandem-l: a mission for monitoring earth system dynamics with high resolution sar interferometry. In *Synthetic Aperture Radar (EUSAR), 2010 8th European Conference on*, pages 1–4. VDE.

[Lillestøl et al., 2001] Lillestøl, E., Hunderi, O., and Lien, J. R. (2001). *Generell fysikk,Bind 2 Varmelære og elektromagnetisme*. Universitetsforlaget.

[Lo, 2002] Lo, S. (2002). Finite element mesh generation and adaptive meshing. *Progress in Structural Engineering and Materials*, 4(4):381–399.

[Lorrain and Corson, 1970] Lorrain, P. and Corson, D. (1970). *Electromagnetic fields and waves*. W.H. Freeman and Company.

[Malmgren et al., 1927] Malmgren, F., Institutt, G., Forskningsfond, S., and Fond, N. V. (1927). *On the properties of sea-ice*. AS John Griegs Boktrykkeri.

[Manninen, 1992] Manninen, A. (1992). Effects of ice ridge properties on calculated surface backscattering in bepers-88. *International Journal of Remote Sensing*, 13(13):2469–2487.

[Marburg, 2002] Marburg, S. (2002). Six boundary elements per wavelength: is that enough? *Journal of Computational Acoustics*, 10(01):25–51.

[Matzler and Wegmuller, 1987] Matzler, C. and Wegmuller, U. (1987). Dielectric properties of freshwater ice at microwave frequencies. *Journal of Physics D: Applied Physics*, 20(12):1623.

[Michéa and Komatitsch, 2010] Michéa, D. and Komatitsch, D. (2010). Accelerating a three-dimensional finite-difference wave propagation code using gpu graphics cards. *Geophysical Journal International*, 182(1):389–402.

[Notur, 2013] Notur (2013). Stallo - Resource description. http://docs.notur.no/uit/stallo_documentation/user_guide/key-numbers-about-stallo. Accessed: 2014-05-14.

[Nyfors, 1982] Nyfors, E. (1982). On dielectric properties of dry snow in the 800 mhz to 13 ghz region. *Helsinki University of Technology. Radio Laboratory, Rep. S*, 13:1982.

[Oh et al., 1992] Oh, Y., Sarabandi, K., and Ulaby, F. T. (1992). An empirical model and an inversion technique for radar scattering from bare soil surfaces. *Geoscience and Remote Sensing, IEEE Transactions on*, 30(2):370–381.

[Oliver and Quegan, 2004] Oliver, C. and Quegan, S. (2004). *Understanding Synthetic Aperture Radar Images*. SciTech Publishing.

[Onstott, 1992] Onstott, R. G. (1992). Sar and scatterometer signatures of sea ice. *Geophysical Monograph Series*, 68:73–104.

[Paterson et al., 1991] Paterson, J., Brisco, B., Argus, S., and Jones, G. (1991). In situ measurements of micro-scale surface roughness of sea ice. *Arctic*, 44(5):140–146.

[Perovich and Gow, 1996] Perovich, D. K. and Gow, A. J. (1996). A quantitative description of sea ice inclusions. *Journal of Geophysical Research: Oceans (1978–2012)*, 101(C8):18327–18343.

[Peterson et al., 1998] Peterson, A. F., Ray, S. L., and Mittra, R. (1998). *Computational methods for electromagnetics*, volume 24. IEEE press New York.

[Petrich and Eicken, 2010] Petrich, C. and Eicken, H. (2010). Growth, structure and properties of sea ice. *Sea Ice*, 2:23–77.

[Phillips, 1989] Phillips, O. (1989). On radar returns from the sea surface—bragg scattering and breaking waves. In *Seventeenth Symposium on Naval Hydrodynamics: Wakes, Free Surface Effects, Boundary Layers and Viscous Flows, Two-phase Flow, Propeller/appendage/hull Interaction*, page 5. National Academies.

[Polder and Van Santeen, 1946] Polder, D. and Van Santeen, J. (1946). The effective permeability of mixtures of solids. *Physica*, 12(5):257–271.

[Quek and Liu, 2003] Quek, S. and Liu, G. (2003). *Finite Element Method: A Practical Course: A Practical Course*. Butterworth-Heinemann.

[Rayleigh, 1899] Rayleigh, J. W. S. B. (1899). *Scientific Papers: 1869-1881*, volume 1. At the University Press.

[Rees, 2005] Rees, W. G. (2005). *Remote sensing of snow and ice*. CRC Press.

[Rice, 1951] Rice, S. O. (1951). Reflection of electromagnetic waves from slightly rough surfaces. *Communications on pure and applied mathematics*, 4(2-3):351–378.

[Richmond, 1965] Richmond, J. H. (1965). Digital computer solutions of the rigorous equations for scattering problems. *Proceedings of the IEEE*, 53(8):796–804.

[Rignot, 2008] Rignot, E. (2008). Changes in west antarctic ice stream dynamics observed with alos palsar data. *Geophysical Research Letters*, 35(12).

[Rosenqvist et al., 2014] Rosenqvist, A., Shimada, M., Suzuki, S., Ohgushi, F., Tadono, T., Watanabe, M., Tsuzuku, K., Watanabe, T., Kamijo, S., and Aoki, E. (2014). Operational performance of the alos global systematic acquisition strategy and observation plans for alos-2 palsar-2. *Remote Sensing of Environment*.

[Sandven et al., 2006] Sandven, S., Johannessen, O. M., and Kloster, K. (2006). Sea ice monitoring by remote sensing. *Encyclopedia of Analytical Chemistry*.

[Serreze and Francis, 2006] Serreze, M. C. and Francis, J. A. (2006). The

arctic on the fast track of change. *Weather*, 61(3):65–69.

[Shokr, 1998] Shokr, M. E. (1998). Field observations and model calculations of dielectric properties of arctic sea ice in the microwave c-band. *Geoscience and Remote Sensing, IEEE Transactions on*, 36(2):463–478.

[Stogryn and Desargant, 1985] Stogryn, A. and Desargant, G. (1985). The dielectric properties of brine in sea ice at microwave frequencies. *Antennas and Propagation, IEEE Transactions on*, 33(5):523–532.

[Stratton, 2007] Stratton, J. A. (2007). *Electromagnetic theory*, volume 33. John Wiley & Sons.

[Stutzman and Thiele, 2012] Stutzman, W. L. and Thiele, A. G. (2012). *Antenna Theory and Design*. John Wiley & Sons.

[Tsang et al., 2000] Tsang, L., Kong, J. A., and Ding, K.-H. (2000). *Scattering of Electromagnetic Waves, Theories and Applications*. John Wiley & Sons.

[Tsang et al., 2001] Tsang, L., Kong, J. A., Ding, K.-H., and Ao, C. O. (2001). *Scattering of electromagnetic waves, numerical simulations*. John Wiley & Sons.

[Tucker III et al., 1992] Tucker III, W., Perovich, D. K., Gow, A. J., Weeks, W. F., and Drinkwater, M. R. (1992). Physical properties of sea ice relevant to remote sensing. *Geophysical Monograph Series*, 68:9–28.

[Vant et al., 1978] Vant, M., Ramseier, R., and Makios, V. (1978). The complex-dielectric constant of sea ice at frequencies in the range 0.1–40 ghz. *Journal of Applied Physics*, 49(3):1264–1280.

[Weeks and Ackley, 1986] Weeks, W. F. and Ackley, S. F. (1986). *The growth, structure, and properties of sea ice*. Springer.

[Winebrenner et al., 1992] Winebrenner, D. P., Bredow, J., Fung, A. K., Drinkwater, M. R., Nghiem, S., Gow, A. J., Perovich, D. K., Grenfell, T. C., Han, H. C., Kong, J. A., et al. (1992). Microwave sea ice signature modeling. *Microwave remote sensing of sea ice*, pages 137–175.

[Yamaguchi et al., 2005] Yamaguchi, Y., Moriyama, T., Ishido, M., and Yamada, H. (2005). Four-component scattering model for polarimetric sar image decomposition. *Geoscience and Remote Sensing, IEEE Transactions on*, 43(8):1699–1706.

[Yang and Altermatt, 2008] Yang, Y. and Altermatt, P. P. (2008). Simulation of optical properties of the si/sio2/al interface at the rear of industrially fabricated si solar cells. In *Proc. of the COMSOL Conference*.

Appendices

A

Brine Volume

This appendix explains the origin of the equation used to calculate brine volume (equation 2.1) and is based on [Cox and Weeks, 1983]. To understand the equation it is important to remember that sea ice is composed of pure ice, brine, solid salts as well as gas, where the salinity of sea ice and the brine salinity are defined as

$$S_i = \frac{m_s}{M} = \frac{m_s^b + m_s^{ss}}{m_b + m_{ss} + m_i} \tag{A.1}$$

and

$$S_b = \frac{m_s^b}{m_b} \, , \tag{A.2}$$

respectively, where M represents the total mass and m_s, m_{ss}, m_b and m_i represent the mass of the salt, the solid salts, the brine and the pure ice, respectively. The superscripts ss in m_s^{ss} and b in m_s^b represent the medium that is considered, such that m_s^{ss} represents the mass of salt in the solid salts and m_s^b represent the mass of salt in the brine. If no upper index is supplied the medium considered is the actual sea ice.

Since

$$m_b = \rho_b V_b \tag{A.3}$$

and

$$M = \rho V \, , \tag{A.4}$$

where ρ represents the density and V the volume, the equations can be combined to

$$\frac{V_b}{V} = \frac{\rho S_i}{\rho_b S_b}\left(\frac{1}{1+\zeta}\right) , \tag{A.5}$$

where

$$\zeta = \frac{m_s^{ss}}{m_s^b} . \tag{A.6}$$

Equation (A.5) can be expressed as

$$\frac{V_b}{V} = \frac{\rho S_i}{F_1(T)} , \tag{A.7}$$

where

$$F_1(T) = \rho_b S_b (1+\zeta) . \tag{A.8}$$

The coefficient, suggested by [Cox and Weeks, 1983], for $F_1(T)$ can be found in Table A.1

Table A.1: Coefficients for $F_1(T)$ as found by [Cox and Weeks, 1983]

T,°C	a_1	a_2	a_3	a_4
$0 \geq T > -2$	−0.041221	−18.407	0.58402	0.21454
$-2 \geq T \geq -22.9$	−4.732	−22.45	−0.6397	−0.01074

B

Small Perturbation Model

This appendix provides information on the SPM and is based on [Fung and Chen, 2010].

The small perturbation surface backscatter model is a model that is applicable for surfaces with small surface roughness relative to the radar wavelength and relies on expanding the scattered field in a Fourier series of plane waves. These waves have different propagation directions and their boundary conditions can be solved using perturbation series [Carlström, 1995].

The roughness is a measure of the surface height standard deviation σ and the surface roughness spectrum as well as the correlation length of the surface, which is denoted with L [Fung and Chen, 2010]. The general form of the backscatter coefficients for horizontal (σ_{HH}), vertical (σ_{VV}) and cross polarized scattering (σ_{VH}) according to the small perturbation theory can be

expressed as follows

$$\sigma^0_{VV} = (4k^4\sigma^2 cos^4\theta)|(\epsilon_r - 1)[(\mu_r\epsilon_r - sin^2\theta) + \epsilon_r \sin^2\theta] + \epsilon_r^2(\mu_r - 1)|^2 \frac{W(2ksin\theta, 0)}{[\pi(\epsilon_r cos\theta + \sqrt{\mu_r\epsilon_r - sin^2\theta})^4} \tag{B.1}$$

$$\sigma^0_{HH} = (4k^4\sigma^2 cos^4\theta)|(\mu_r - 1)[(\mu_r\epsilon_r - sin^2\theta) + \mu_r \sin^2\theta] + \mu_r^2(\epsilon_r - 1)|^2 \frac{W(2ksin\theta, 0)}{[\pi(\mu_r cos\theta + \sqrt{\mu_r\epsilon_r - sin^2\theta})^4} \tag{B.2}$$

$$\sigma^0_{VH} = \frac{S(\theta)}{2\pi^3} k^8\sigma^4 cos^2\theta|(\epsilon_r - 1)(R_{\|} - R_{\perp})|^2 \int_0^{2\pi}\int_0^{1-} \left|\frac{S(v)v^2 cos\phi sin\phi}{\epsilon_r\sqrt{1-v^2} + \sqrt{\epsilon_r - v^2}}\right|^2 W_1 W_2 v\partial v\partial\phi \tag{B.3}$$

where W, W_1 and W_2 are surface spectra, also referred to as roughness spectrum [Rice, 1951], evaluated at different spectral values. These surface spectra are the two dimensional Fourier transforms of the correlation coefficient of the surface $p(x, y)$ and are found in the following way

$$W_1 = W[k(vcos\varphi - sin\theta), kvsin\varphi] \tag{B.4}$$

$$W_2 = W[k(vcos\varphi + sin\theta), kvsin\varphi] \tag{B.5}$$

where the rectangular and polar form W are defined as:

$$W(k_x, k_y) = \int_{-\infty}^{\infty}\int_{-\infty}^{\infty} p(x, y)e^{-jk_x x - jk_y y}\partial x\partial y \tag{B.6}$$

$$W(\kappa, \varphi) = \int_0^{2\pi}\int_0^{\infty} p(r, \phi)e^{-j\kappa r cos(\varphi - \phi)} r\partial r\partial\phi \tag{B.7}$$

κ in these expression originates from the wavenumber ($\kappa = \sqrt{k_x^2 + k_y^2}$). In cases where roughness is not dependent on the view direction the correlation coefficient is only dependent on the radial variable r and B.7 can be simplified to

$$w(\kappa) = 2\pi \int_0^{\infty} p(r) J_0(\kappa r) r\partial r \tag{B.8}$$

where $J_0(\kappa r)$ denotes the Bessel function of zeroth-order.

$S(\theta)$ and $S(v)$ in equation B.3 denote the shadowing functions. These functions are only accurate for high frequency conditions and geometric optics and are still a focus of current research. Due to the fact that small perturbation surface

modeling only focuses on slightly rough surfaces, the single scattering calculations usually do not require the use of shadowing functions. They are however required for very large incidence angles. They are also required, for multiple scattering calculations, since the source for the phenomenon of multi scattering is the shadowed field [Fung and Chen, 2010].

Due to the fact that most surfaces in nature consist of roughness of different scales it can generally be assumed that for large sampling intervals the correlation function appears exponentially [Fung and Chen, 2010]. Assuming such a exponential correlation the surface spectra can be found in the following way

$$W(2ksin\theta) = \frac{2\pi L^2}{(1 + (2kLsin\theta)^2)^{3/2}} \tag{B.9}$$

$$W_1[k\sqrt{(vcos\varphi - sin\theta)^2 + (vsin\varphi)^2}] = \frac{2\pi L^2}{\left(1 + (kL)^2\left((vcos\varphi - sin\theta)^2 + (vsin\varphi)^2\right)\right)^{3/2}} \tag{B.10}$$

$$W_2[k\sqrt{(vcos\varphi + sin\theta)^2 + (vsin\varphi)^2}] = \frac{2\pi L^2}{\left(1 + (kL)^2\left((vcos\varphi + ksin\theta)^2 + (vsin\varphi)^2\right)\right)^{3/2}} \tag{B.11}$$

C

Reflection for 3-layer media

This appendix contains the derivation of equation (4.36), which is used to find the reflection of a 3-layer medium as seen in Figure C.1.

It can be seen from Figure C.1 that the total reflected wave consists of infinitely many components due to the reflections in the middle layer. Using the Fresnel equations the reflection and transmission coefficients can be found at each boundary, however, since the wave components that travel through the medium travel a longer distance than for the first component it is important to also take into account the phase difference as well as the attenuation. For one length through the medium this can be expressed as

$$e^{j(n_2 k)dcos(\theta_2)} , \tag{C.1}$$

where k is the wavenumber

$$k = \frac{2\pi}{\lambda} , \tag{C.2}$$

θ_2 denotes the angle at which the wave propagates in the second medium, λ is the wavelength, and d is the thickness of the second layer.

Looking at the infinite summation of reflected wave components it can be seen that the first component can be expressed as

$$E_r^{(1)} = E_i r_{12} . \tag{C.3}$$

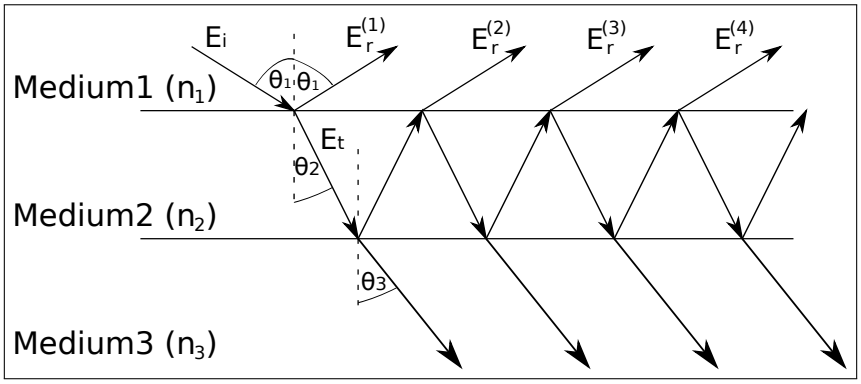

Figure C.1: Displays the incidence, transmitted and reflected part of the **E**-field for the three layer structure. The incidence angle for the top surface is denoted θ_1, whereas the angle of incidence for the second surface is denoted with θ_2. The refractive indices are n_1,n_2 and n_3 (top to bottom).

Similarly the second one can be expressed, by using the Fresnel equations at the various interfaces and accounting for the travel through the medium (both ways), as

$$E_r^{(2)} = E_i t_{12} r_{23} t_{21} e^{2j(n_2 k) d cos(\theta_2)} \ . \tag{C.4}$$

For the third contribution it will be

$$E_r^{(3)} = E_i t_{12} r_{23} t_{21} e^{2j(n_2 k) d cos(\theta_2)} (r_{23} r_{21} e^{2j(n_2 k) d cos(\theta_2)}) \ . \tag{C.5}$$

Inspecting the first three contributions and noticing the repeating pattern, it can be seen that the total contribution from the 2 to m^{th} components can be generalized as

$$E_r^{(2-m^{th})} = E_i t_{12} e^{2j(n_2 k) d cos(\theta_2)} r_{23} t_{21} \sum_{m=0}^{\infty} (r_{23} r_{21} e^{2j(n_2 k) d cos(\theta_2)})^m \ . \tag{C.6}$$

Noticing the geometric series in the above equation the total reflection can be written as

$$r = r_{12} + \frac{t_{12} e^{2j(n_2 k) d cos(\theta_2)} r_{23} t_{21}}{1 - r_{23} r_{21} e^{2j(n_2 k) d cos(\theta_2)}} \ . \tag{C.7}$$

Making use of the fact that $r_{21} = -r_{12}$ and rearranging the equation results in

$$r = \frac{r_{12} + (t_{12}t_{21} - r_{12}r_{21})e^{2j(n_2k)dcos(\theta_2)}r_{23}}{1 + r_{12}r_{23}e^{2j(n_2k)dcos(\theta_2)}} , \tag{C.8}$$

which by using $t_{12}t_{21} - r_{12}r_{21} = 1$ can be written as

$$r = \frac{r_{12} + e^{2j(n_2k)dcos(\theta_2)}r_{23}}{1 + r_{12}r_{23}e^{2j(n_2k)dcos(\theta_2)}} . \tag{C.9}$$

These steps are valid for both polarizations and equation (C.9) can therefore be written as equation (4.36).